Fluorescent Silicon Carbide and its Applications in White Light-Emitting Diodes

Ou, Yiyu; Ou, Haiyan

Publication date:
2012

Document Version
Publisher's PDF, also known as Version of record

Fluorescent Silicon Carbide and its Applications in White Light-Emitting Diodes

Ph.D. Thesis

Yiyu Ou
欧亦宇

December, 2012

DTU Fotonik
Department of Photonics Engineering
Technical University of Denmark
DK-2800 Kgs. Lyngby
Denmark

"Your theory is crazy, but it's not crazy enough to be true."

– Niels Bohr

Preface

The work presented in this thesis has been carried out as my Ph.D. project in the period of February 1^{st} 2010–January 31^{st} 2013. The work took place mainly at Department of Photonics Engineering (DTU Fotonik), Technical University of Denmark. A two and half month research stay was spent at Department of Materials Science and Engineering at Meijo University, Japan. The project was financed by the Danish councils for strategic research funding through project "Nordic Light Emitting Diode Initiative (NORLED)" (project no. 09-072118). Main supervisor of my Ph.D. project is Dr. Haiyan Ou, Associate Professor at DTU Fotonik, Technical University of Denmark.

Acknowledgement

During the last three years as a Ph.D. student at DTU Fotonik I have received help from many people to whom I would like to express my gratitude. This work could not have been done without collaboration with and help from you.

First I would like to thank my supervisor Prof. Haiyan Ou, for giving me this opportunity to work at DTU Fotonik as a Ph.D. student, for her insightful guidance and fruitful discussions throughout the project, and also for so much support and encouragement. Haiyan has been a great supervisor as well as a wonderful friend. Thank you for sharing your knowledge and I have learnt a lot from you indeed.

Warm gratitude to Valdas Jokubavicius, Prof. Mikael Syväjärvi, Dr. Jianwu Sun and Prof. Rositza Yakimova from Linköping University for the great collaboration within NORLED project. Special thanks to Valdas for growing so many high-quality SiC wafers for me in the last three years.

I am also grateful to Prof. Satoshi Kamiyama from Meijo University for providing me a great opportunity to work in his group on Porous SiC project. Many thanks to Takahiro Takahashi for experimental assistance during my stay in Meijo University.

Sincere thanks to Dennis Dan Corell, Dr. Carsten Dam-Hansen and Prof. Paul Michael Petersen for the collaboration on the colorimetry research of the subwavelength structures. Thanks to Dr. Rolf Berg and Dr. Chuan Liu from DTU Chemistry for the collaboration on the Raman spectroscopy. Thanks to Xiaolong Zhu, Dr. Sanshui Xiao, and Prof. N. Asger Mortensen for the collaboration on the nanosphere patterning.

Many thanks to Dr. Peixiong Shi and Dr. Katharina Nilson from DTU Danchip for sharing their experience and giving process assistance. Thanks to Dr. Yaohui Chen, Hairun Guo and Xiaolong Zhu for all the valuable discussion and assitance on the simulation work. Thanks to

Dr. Yuxin Song from Chalmers University of Technology for the help on LTPL measurement.

I would also like to thank all my friends, colleagues and office mates. I will remember those good time we spent together.

Danish councils for strategic research funding is acknowledged for the financial support through NORLED project.

Last but not least, I would like to thank my parents and my wife Yiqi. Thank you for your unconditional love and constant support during all these years. I hope this makes you pround.

Abstract

This thesis focuses on the optical properties analysis of Donor-Acceptor-Pair (DAP) co-doped Fluorescent Silicon Carbide (f-SiC) as a wavelength-conversion material in white Light-Emitting Diodes (LEDs). Different methods of fabricating surface Antireflective Structures (ARS) on f-SiC to enhance its light extraction efficiency are presented.

White LEDs are the most promising techniques to replace the conventional lighting sources. A typical white LED consists of a Gallium Nitride (GaN) blue or Ultraviolet (UV) LED stack and a wavelength-conversion material. Silicon Carbide (SiC) has a wide optical bandgap and could be tailored to emit light at different wavelength by introducing different dopants. Combined emitting spectra of two types of DAP co-doped f-SiC could cover the whole visible spectral range and make f-SiC as a good candidate of wavelength-conversion material. It has a better color rendering performance and a much longer material lifetime compared with the commonly used wavelength-conversion material like Phosphors. In this thesis, f-SiC with different doping concentrations are analyzed and optimized in order to enhance the quantum efficiency.

On the other hand, semiconductor materials usually suffer from the low light extraction efficiency due to the large refractive index difference between air and semiconductor interface. To ease this limitation, ARS have been widely applied on the semiconductor surface in LED and solar cell applications. This thesis has theoretically investigated the impact of surface ARS on colorimetry and light extraction efficiency of f-SiC based white LED. Furthermore, various approaches of fabricating periodic and pseudoperiodic ARS are demonstrated. By introducing ARS, a significant surface reflection suppression and a considerable omnidirectional luminescence enhancement have been observed.

Resumé

Denne afhandling fokuserer på analysering af de optiske egenskaber ved Donor-Acceptor-Par (DAP) co-doperet Fluorescerende Silicium Carbide (f-SiC) som bølgelængde konvertering i hvide lysdioder (LED'er). Alternativ fabrikationsmetoder af Antireflekterende Strukturer (ARS) på f-SiC er præsenteret, med det formål at lys ekstraktionen forbedres.

Hvide LED'er er de mest lovende til at erstatte de konventionelle lyskilder. En typisk hvid LED består af blå eller ultraviolette Gallium Nitrid (GaN) LED stak og en bølgelængde-konverterings materiale. Det brede optiske båndgab i Silicium Carbide (SiC) gør det muligt at designe materialet til at udsende lys med forskellige bølgelængder ved at introducere forskellige doping produkter. De sammenlagte spektre af to typer DAP co-doperet f-SiC er i stand til at dække hele det synlige spektrum og gør f-SiC den førende kandidat af bølgelængde-konverterings materiale. Den har en overlegen farvegengivelse og længere materiale levetid sammenlignet med de ofte anvendte bølgelængde-konverterings materialer som fosfor. I denne afhandling er f-SiC med forskellige dopering analyseret og optimeret for at forbedre kvante-effektiviteten.

På den anden side medfører den høje brydningsindeksforskel mellem halvleder and luft, at halvleder materialer har en meget lav lys ekstraktion. ARS er ofte blevet anvendt i LED og solcelle applikationer på halvleder overfladen for at overkomme denne ulempe. Denne afhandling har teoretisk undersøgt effekten af overflade ARS på kolorimetri og lys ekstraktionen af f-SiC baseret på hvid LED. Yderligere er forskellige metoder til fabrikation af periodiske og pseudo-periodiske ARS blevet præsenteret. Introduktionen af ARS har vist en betydelig nedsættelse af overfalderefleksion samt retningsuafhængige forstærkning af luminescens.

Ph.D. Publication List

Journals articles

1. **Y. Ou**, I. Aijaz, V. Jokubavicius, R. Yakimova, M. Syväjärvi, and H. Ou, "Broadband antireflection silicon carbide surface by self-assembled nanopatterned reactive-ion etching," Optical Materials Express **3**(1), 86-94 (2013).

2. **Y. Ou**, V. Jokubavicius, M. Kaiser, P. Wellmann, M. K. Linnarsson, R. Yakimova, M. Syväjärvi, and H. Ou, "Fabrication of broadband antireflective sub-wavelength structures on fluorescent SiC," Materials Science Forum **740-742**, 1024-1027 (2013).

3. M. Wilhelm, M. Kaiser, V. Jokubavicius, M. Syväjärvi, **Y. Ou**, H. Ou, and P. Wellmann, "Photoluminescence topography of fluorescent SiC and its corresponding source crystals," Materials Science Forum **740-742**, 421-424 (2013).

4. M. K. Linnarsson, M. Kaiser, R. Liljedahl, V. Jokubavicius, S. Schimmel, M. Syväjärvi, **Y. Ou**, H. Ou, and P. Wellmann, "Lateral boron distribution in polycrystalline SiC source for growth of fluorescent 6H-SiC," Materials Science Forum **740-742**, 397-400 (2013).

5. S. Schimmel, M. Kaiser, P. Hens, V. Jokubavicius, R. Liljedahl, J. Sun, R. Yakimova, **Y. Ou**, H. Ou, M. K. Linnarsson, P. Wellmann, and M. Syväjärvi, "Step-flow growth of fluorescent 4H-SiC layers on 4 degree off-axis substrates," Materials Science Forum **740-742**, 185-188 (2013).

6. M. Kaiser, T. Hupfer, V. Jokubavicius, S. Schimmel, M. Syväjärvi, **Y. Ou**, H. Ou, M. K. Linnarsson, and P. Wellmann, "Polycrys-

talline SiC as source material for the growth of fluorescent SiC layers," Materials Science Forum **740-742**, 39-42 (2013).

7. X. Zhu, **Y. Ou**, H. Ou, O, Hansen, N. A. Mortensen, and S. Xiao, "Broadband light-extraction enhancement by using a whispering gallery resonators array," Applied Physics Letters **101**(24), 241108 (2012).

8. **Y. Ou**, V. Jokubavicius, R. Yakimova, M. Syväjärvi, and H. Ou, "Omnidirectional luminescence enhancement of fluorescent SiC via pseudo-periodic antireflective sub-wavelength structures," Optics Letters **37**(18), 3816-3818 (2012).

9. **Y. Ou**, V. Jokubavicius, P. Hens, M. Kaiser, P. Wellmann, R. Yakimova, M. Syväjärvi, and H. Ou, "Broadband and omnidirectional light harvesting enhancement of fluorescent SiC," Optics Express **20**(7), 7575-7579 (2012).

10. **Y. Ou**, V. Jokubavicius, C. Liu, R. W. Berg, M. K. Linnarsson, S. Kamiyama, Z. Lu, R. Yakimova, M. Syväjärvi, and H. Ou, "Photoluminescence and Raman spectroscopy characterization of boron- and nitrogen-doped 6H silicon carbide," Materials Science Forum **717-720**, 233-236 (2012).

11. **Y. Ou**, V. Jokubavicius, M. K. Linnarsson, R. Yakimova, M. Syväjärvi, and H. Ou, "Characterization of donor-acceptor-pair emission in fluorescent 6H-SiC," Physica Scripta **T148**, 014003 (2012).

12. M. Syväjärvi, J. Müller, J. Sun, V. Grivickas, **Y. Ou**, V. Jokubavicius, P. Hens, M. Kaisr, K. Ariyawong, K. Gulbinas, P. Hens, R. Liljedahl, M. K. Linnarsson, S. Kamiyama, P. Wellmann, E. Spiecker, and H. Ou, "Fluorescent SiC as new material for white LEDs," Physica Scripta **T148**, 014002 (2012).

13. **Y. Ou**, V. Jokubavicius, S. Kamiyama, C. Liu, R. Berg, M. K. Linnarsson, R. Yakimova, M. Syväjärvi, and H. Ou, "Donor-acceptor-pair emission characterization in N-B doped fluorescent SiC," Optical Materials Express **1**(8), 1439-1446 (2011).

14. H. Ou, **Y. Ou**, C. Liu, R. Berg, and K. Rottwitt, "Formation and characterization of varied size germanium nanocrystals by electron

microscopy, Raman spectroscopy, and photoluminescence," Optical Materials Express **1**(4), 643-651 (2011).

15. **Y. Ou**, D. Corell, C. Dam-Hansen, P. Petersen, and H. Ou, "Antireflective sub-wavelength structures for improvement of the extraction efficiency and color rendering index of monolithic white light-emitting diode," Optics Express **19**(S2), A166-A172 (2011).

16. V. Jokubavicius, R. Liljedahl, **Y. Ou**, H. Ou, S. Kamiyama, R. Yakimova, and M. Syväjärvi, "Geometrical control of 3C and 6H-SiC nucleation on low off-axis substrates," Materials Science Forum **679-680**, 103-106 (2011).

Conference contributions

1. S. Schimmel, M. Kaiser, V. Jokubavicius, **Y. Ou**, P. Hens, M. K. Linnarsson, J. Sun, R. Liljedahl, H. Ou, P. Wellmann, and M. Syväjärvi, "The role of defects in fluorescent silicon carbide layers grown by sublimation epitaxy," European Materials Research Society 2013 Spring Meeting, Strasbourg, France (2013).

2. V. Jokubavicius, J. Sun, M. K. Linnarsson, R. Liljedahl, M. Kaiser, P. Wellmann, **Y. Ou**, H. Ou, R. Yakimova, and M. Syväjärvi, "Stability and doping of 3C-SiC: from thin film to bulk growth," European Materials Research Society 2013 Spring Meeting, Strasbourg, France (2013).

3. H. Ou, **Y. Ou**, S. Kamiyama, M. Kaiser, P. Wellmann, M. K. Linnarsson, V. Jokubavicius, R. Yakimova, and M. Syväjärvi, "Fluorescent SiC for white light-emitting diodes," Asia Communications and Photonics Conference 2012, Guangzhou, China (2012). **(invited talk)**

4. M. Syväjärvi, J. Sun, P. Wellmann, V. Jokubavicius, S. Schimmel, P. Hens, R. Liljedahl, R. Yakimova, M. Kaiser, M. Wilhelm, M. K. Linnarsson, **Y. Ou**, and H. Ou, "Fluorescent SiC as a new platform for visible and infrared emitting applications as well as prospective photovoltaics," Materials Research Society 2012 Fall Meeting, Boston, USA (2012).

5. M. Kaiser, T. Hupfer, V. Jokubavicius, S. Schimmel, M. Syväjärvi, **Y. Ou**, H. Ou, M. K. Linnarsson, and P. Wellmann, "Polycrystalline SiC as source material for the growth of fluorescent SiC

layers," European Conference on Silicon Carbide and Related Materials 2012, Saint Petersburg, Russia (2012).

6. **Y. Ou**, V. Jokubavicius, M. Kaiser, P. Wellmann, M. K. Linnarsson, R. Yakimova, M. Syväjärvi, and H. Ou, "Fabrication of broadband antireflective sub-wavelength structures on fluorescent SiC," European Conference on Silicon Carbide and Related Materials 2012, Saint Petersburg, Russia (2012).

7. S. Schimmel, M. Kaiser, P. Hens, V. Jokubavicius, R. Liljedahl, J. Sun, R. Yakimova, **Y. Ou**, H. Ou, M. K. Linnarsson, P. Wellmann, and M. Syväjärvi, "Step-flow growth of fluorescent 4H-SiC layers on 4 degree off-axis substrates," European Conference on Silicon Carbide and Related Materials 2012, Saint Petersburg, Russia (2012).

8. M. K. Linnarsson, M. Kaiser, R. Liljedahl, V. Jokubavicius, S. Schimmel, M. Syväjärvi, **Y. Ou**, H. Ou, and P. Wellmann, "Lateral boron distribution in polycrystalline SiC source for growth of fluorescent 6H-SiC," European Conference on Silicon Carbide and Related Materials 2012, Saint Petersburg, Russia (2012).

9. M. Wilhelm, M. Kaiser, V. Jokubavicius, M. Syväjärvi, **Y. Ou**, H. Ou, and P. Wellmann, "Photoluminescence topography of fluorescent SiC and its corresponding source crystals," European Conference on Silicon Carbide and Related Materials 2012, Saint Petersburg, Russia (2012).

10. **Y. Ou**, I. Aijaz, and H. Ou, "Fluorescent SiC with pseudo-periodic moth-eye structures," SPIE Optics + Photonics 2012, San Diego, USA (2012).

11. P. Wellmann, M. Kaiser, T. Hupfer, J. Sun, V. Jokubavicius, P. Hens, R. Liljedahl, M. Syväjärvi, **Y. Ou**, H. Ou and M. K. Linnarsson, "Crystal growth and characterization of fluorescent SiC," European Conference on Crystal Growth, Glasgow, UK (2012).

12. H. Ou, **Y. Ou**, S. Kamiyama, M. Kaiser, P. Wellmann, M. K. Linnarsson, V. Jokubavicius, R. Yakimova, and M. Syväjärvi, "Fluorescent SiC based all semiconductor white LED," Sino-Swedish Workshop on Sustainable and Energy Efficient Device Technology, Gothenburg, Sweden (2012).

13. **Y. Ou**, V. Jokubavicius, R. Yakimova, M. Syväjärvi, and H. Ou, "Enhanced extraction efficiency of fluorescent SiC by surface nanostructuring," Conference on Lasers and Electro-Optics 2012, San Jose, USA (2012).

14. H. Ou, D. Corell, **Y. Ou**, P. Poulsen, C. Dam-Hansen, P. Petersen, "Spectral design flexibility of LED brings better life," Photonics West 2012, San Francisco, USA (2012). **(invited talk)**

15. V. Grivickas, K. Gulbinas, V. Jokubavicius, J. Sun, **Y. Ou**, H. Ou, M. K. Linnarsson, M. Syväjärvi, and S. Kamiyama, "Carrier lifetimes in fluorescent 6H-SiC for LEDs application," Lithuanian National Physics Conference 2011, Vilnius, Lithuania (2011).

16. **Y. Ou**, V. Jokubavicius, C. Liu, R. Berg, M. K. Linnarsson, S. Kamiyama, Z. Lu, R. Yakimova, M. Syväjärvi, and H. Ou, "Photoluminescence and Raman spectroscopy characterization of boron- and nitrogen-doped 6H silicon carbide," International Conference on Silicon Carbide and Related Materials 2011, Cleveland, USA (2011).

17. **Y. Ou**, V. Jokubavicius, M. K. Linnarsson, R. Yakimova, M. Syväjärvi, and H. Ou, "Characterization of donor-acceptor-pair emission in fluorescent 6H-SiC," 24th Nordic Semiconductor Meeting, Århus, Denmark (2011).

18. H. Ou, **Y. Ou**, C. Liu, R. Berg, and K. Rottwitt, "Size-effect of germanium nanocrystals," Conference on Lasers and Electro-Optics 2011, Baltimore, USA (2011).

Award

- 2012 Chinese Government Award for Outstanding Self-Financed Students Abroad

Contents

Chapter 1

Introduction

Silicon Carbide (SiC) has been widely used in high-temperature, high-power, high-frequency, and radiation-resistant applications due to its many well known material properties of high thermal conductivity, large optical bandgap, high saturated electron drift velocity, and high breakdown field. Besides, due to its relatively small lattice mismatch with Gallium Nitride (GaN), it is also an excellent candidate as a substrate material for GaN Light-Emitting Diode (LED) growth.

With the progress of device efficiency and reliability, white LEDs are being widely used and replacing conventional lighting sources over the past decade due to the higher luminous efficacy and longer lifetime. Meanwhilte, white LEDs also have many other promising applications such as the backlight source of liquid crystal flat display panels and the head lights of vehicles [1]. White light sources are normally evaluated in terms of their luminous efficacy of radiation and color rendering properties which is usually represented by Color Rendering Index (CRI), and there is a fundamental trade-off between the luminous efficacy of radiation and color rendering [2].

There are two general ways to realize white LEDs. One approach is by additive color mixing of two or more monochromatic LEDs sources emitting complementary colors. Generally, dichromatic white light source has the highest luminous efficacy and the lowest color rendering index. A trichromatic white light source has acceptable color rendering property and luminous efficacy. However, with increased monochromatic light sources (tetrachromatic and pentachromatic), CRI>90 could be achieved, while the luminous efficacy is much lower [3]. These type of LEDs usually need electronic circuits to control the blending and diffu-

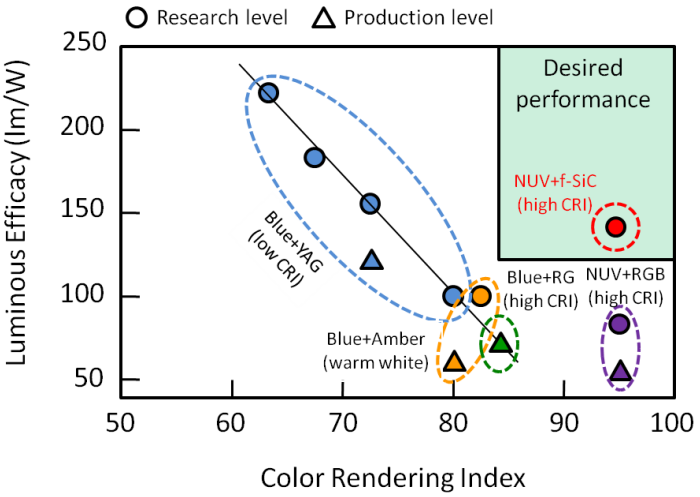

Figure 1.1: Current status of wavelength-conversion material based white LEDs.

sion of different colors, and because the individual color LEDs typically have slightly different emission patterns (leading to variation of the color depending on direction) even if they are made as a single unit, these are seldom used to produce white lighting. In addition, their emission power decays exponentially with rising temperature, resulting in a substantial change in color stability. Nevertheless, this method has the flexibility of mixing different colors as well as higher quantum efficiency in producing white light [3, 4].

The other viable and common method to generate white light is using a blue or Ultraviolet (UV) LED whose light is partially or fully used to optically excite wavelength-conversion materials such as phosphors [5], dyes [6], or semiconductors [1, 7]. As like in white LEDs based on color mixing, with increased number of chromatic light sources, the luminous efficacy decreases but the color rendering capability is improved. The most common wavelength-conversion material is phosphor. A typical phosphor-based white LED is composed of a blue or UV LED with cerium-doped yttrium aluminitum garnet (YAG: Ce). High luminous efficiency and stable performance could be achieved [5, 8–10], however, it suffers from a halo effect of blue/yellow color separation and poor CRI caused by a lack of red component in the spectrum [9, 11–13]. Dyes materials have internal quantum efficiency close to 100%, however, a serious drawback of dyes is lacking of the long-term stability due to their

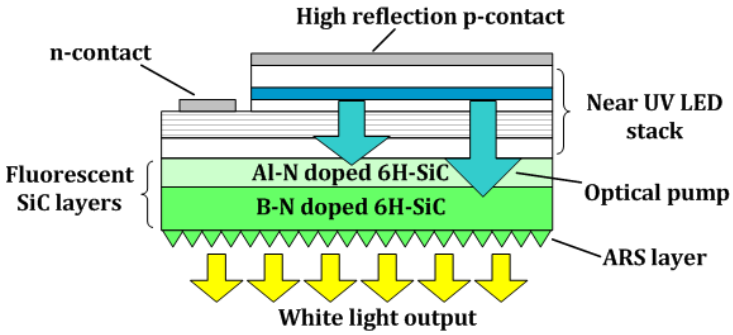

Figure 1.2: Schematic diagram of fluorescent SiC based white LED

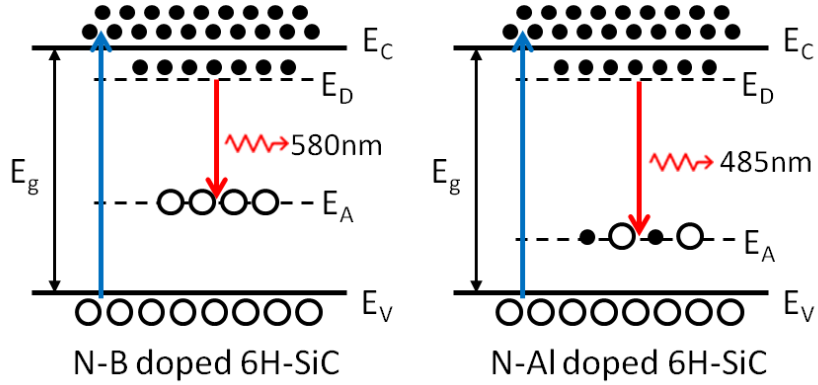

Figure 1.3: Band diagrams of N-B (left) and N-Al (right) doped 6H-SiC under excitation (black dots represent electrons and unfilled circles represent holes).

finite lifetime as organic material. As for its competitors, semicondutors also have internal quantum efficiency near 100%. Other advantages of semiconductor convertors are less severe light escape problem and precise tailor of the emission spectrum [7, 8]. Due to the simplicity of manufacturing and cheaper price, the majority of high-intensity white LEDs presently on the market are manufactured using phosphor light conversion. Fig. 1.1 shows the current status of white LEDs based on different wavelength-conversion technology. Although the fundamental trade-off between the luminous efficacy of radiation and color rendering exists, high-efficiency wavelength-conversion materials with high CRI value and long lifetime are required and indispensable for todays white LEDs applications.

A new monolithic white LED was invented by Kamiyama [1] and

its schematic diagram is demonstrated in Fig. 1.2. It is based on a combination of dual doped Fluorescent Silicon Carbide (f-SiC) epitaxial layers and a near UV LED (NUV-LED) AlGaN stack grown on the 6H-SiC epitaxial layers. The NUV-LED acts as an excitation source and two 6H-SiC epitaxial layers play as wavelength convertor. There is a high-reflection contact on top of the NUV-LED, as a result, most of the NUV light generated in the active layer of the NUV-LED stack goes into the 6H-SiC epitaxial layers.

It is known that, with large optical bandgap, SiC can be tailored to emit light across the entire visible spectrum, as well as the near UV region by introducing different dopants. The first SiC epitaxial layer is co-doped by nitrogen (N) and boron (B) while the second one is co-doped by nitrogen (N) and aluminum (Al). The band diagrams of N-B and N-Al doped 6H-SiC under excitation are presented in Fig. 1.3. The Donor-Acceptor-Pair (DAP) luminescences of N-B doped SiC layer can emit a warm white light with a peak wavelength at around 580 nm. The spectrum from N-Al doped SiC exhibits a blue-green emission (peak at around 485 nm). Combined DAP luminescences of the two f-SiC layers can cover most of the visible spectral range and thus a pure white light with CRI larger than 90 could be produced. The luminous efficiency could reach 130 lm/W, and this is much higher than the efficiency of incandescent lamps, about 10 lm/W and even higher than that of the fluorescent lamp, typically 80 lm/W [5]. The lifetime of this SiC-based white LED could be up to 300 thousand hours which is much longer than typical phosphor-based white LED's 50 thousand hours. Furthermore, SiC is a well-established substrate material for nitride growth and has excellent thermal conductivity. With improved growth technology, better performance is expected.

In this thesis, a study of f-SiC is carried out with the focus on the optical properties analysis and fabrication of surface Antireflective Structures (ARS). Impact of applying surface ARS on f-SiC has been theoretically studied. Several ARS fabrication methods are then demonstrated to enhance the light extraction efficiency.

Chapter 2 gives a brief introduction to SiC. Different polytypes of SiC and their properties are summarized in section 2.1. Various growth, doping and etching methods are discussed in section 2.2. Applications of SiC in LEDs are presented in section 2.3.

Chapter 3 introduces f-SiC and its optical properties. The mechanism of donor-acceptor-pair emission of Nitrogen-Boron doped 6H-SiC

is discussed in section 3.1. Raman spectroscopy and Angle-Resolved Photoluminescence (ARPL) study are presented in section 3.2 and 3.3 respectively.

Chapter 4 presents the modelling results of applying surface ARS on f-SiC by using Rigorous Coupled-Wave Analysis (RCWA) algorithm. In section 4.1, impacts of different ARS types and structure heights on f-SiC based white LED are investigated in terms of CRI, Correlated Color Temperature (CCT) and position in the chromaticity diagram. Structure profile dependent broadband antireflection performance of cone-shaped ARS is systematically studied and discussed in section 4.2.

Chapter 5 presents three methods of fabricating surface ARS on f-SiC. One method to fabricate periodic ARS by using Electron beam (E-beam) lithography mask patterning is introduced in section 5.1. Another way to fabricate periodic ARS by nanosphere lithography mask patterning is demonstrated in section 5.2. A method to fabricate pseudoperiodic ARS by using self-assembled metal nanoparticles as etching mask is introduced in section 5.3. Significant surface antireflection and omnidirectional luminescence enhancement of f-SiC are demonstrated among all these methods.

Chapter 6 summarizes the work in this thesis and makes an outlook on future work.

Chapter 2

Silicon carbide

Silicon Carbide (SiC) is the only binary compound of silicon and carbon in solid state. It exists in a large number of polytypes which differ in their properties. SiC has attracted both research and industrial interest for decades. Owing to the material properties of high thermal conductivity, large optical bandgap, high saturated electron drift velocity, and high breakdown field, SiC is being widely used in high-temperature, high-power, high-frequency, and radiation-resistant applications. Many efforts have been made on the material growth and processing technology of SiC.

2.1 Polytypes and Properties

2.1.1 Polytypes

In SiC compound, one tetrahedrally bonded Si-C bilayer could be represented as one sheet, and each sheet is a close-packed array of spheres with hexagonal symmetry [14]. Along the direction perpendicular to the sheet (c-axis), there are two possible ways to stack an identical second sheet atop the first one, while these possibilities can be represented as occupation sites (hexagonal and cubic sites) which is shown in Fig.2.1. Thus, one sheet can be denoted as A (represent for the first sheet in usual), B or C, depending on the different occupation site. The change of sheet stacking sequence (occupation sites) along the c-axis gives the different polytypes of SiC [15].

Polytypes are determined by the stacking periodicity along the c-axis, and over 200 polytypes of SiC have been discovered [16]. These

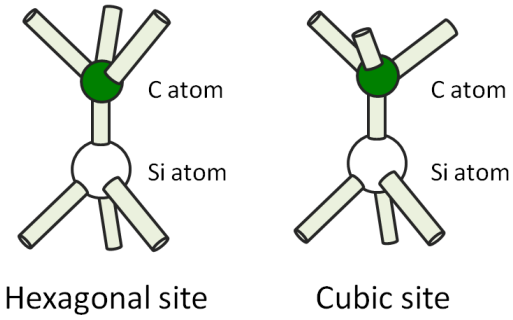

Figure 2.1: Occupation sites (hexagonal and cubic) of Si and C atoms.

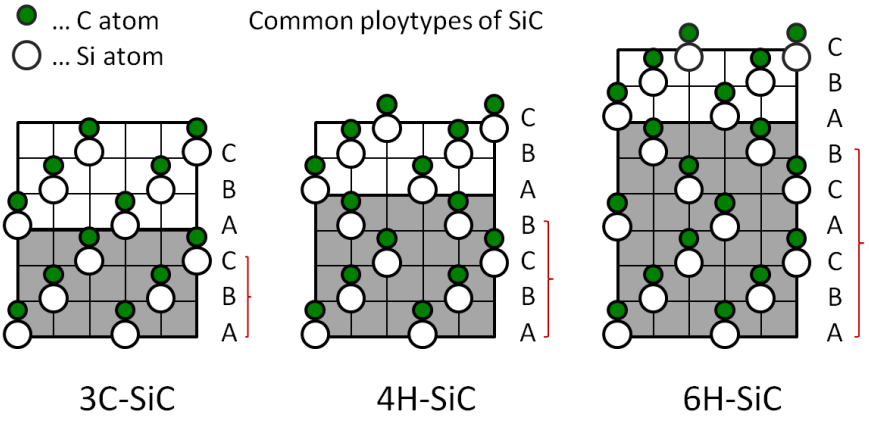

Figure 2.2: Arrangements of Si and C atoms for 3C-, 4H-, and 6H-SiC.

polytypes are named by the number of stacking layers in a unit cell and crystallographic types: cubic (C), hexagonal (H), and rhombohedral (R). Most commonly studied polytypes include 3C-, 4H-, 6H-, and 15R-SiC. 3C-SiC is the only cubic polytype and also referred to β-SiC, whereas the hexagonal and rhombohedral structures are collectively grouped as α-SiC [17]. Examples of atom arrangements of 3C-, 4H-, and 6H-SiC are represented in Fig.2.2.

2.1.2 Properties

Hundreds of polytypes in SiC arise from the difference stacking sequence along the c-axis. Numerous physical and miscellaneous properties of different structure have been investigated during decades.

Table 2.1: Lattice parameters and related properties of SiC

Polytype	n^a	$a(\text{Å})^b$	$c(\text{Å})^c$	c/na	$V(\text{Å}^3)^d$	$d(g/cm^3)^e$
3C [18]	3	3.0827	7.5510	0.8165	62.1438	3.2143
4H [19]	4	3.0730	10.053	0.8178	82.215	3.239
6H [20]	6	3.08086	15.1174	0.8178	124.2658	3.2149
15R [21]	15	3.07	37.70	0.819	307.72	3.24

[a]Number of bilayers in a period.
[b]C-C (or Si-Si) bond length.
[c]Lattice constant.
[d]Unit cell volume, calculated using $V = \frac{a^2 c\sqrt{3}}{2}$.
[e]Density, calculated using $nM/(N_A V)$, where N_A is the Avogadro constant ($6.022 \cdot 10^{23} mol^{-1}$), and M is the Si-C molecular weight ($40.09715g\ mol^{-1}$).

Table 2.1 lists the lattice parameters and related properties of common SiC polytypes. c/na is the ratio between the height of the tetrahedron c/n and the C-C (or Si-Si) bond length a, where c is the lattice parameter, and n specifies the number of bilayers in a period of the polytype. For complete tetrahedral symmetry, all the Si-C bond length should be the same and this gives the c/na value of 0.816496. From table 2.1, it is shown that all polytypes except 3C have larger c/na than the ideal value, which indicate that there is one longer (vertical) bond and three shorter (lateral) bonds in the structure. From the a and c lattice parameters obtained by X-ray data, the unit cell volume V and density d can be calculated. All the measurement results list in table 2.1 were realized at room temperature ($\approx$ 300 K).

Miscellaneous properties of SiC are summarized in table 2.2. In Mohs scale (10), SiC presents high hardness (9), which is much harder than other common materials, such as silicon (7), germanium (6), steel (4.5), and copper (3). In addition, its properties of high thermal conductivity, large optical bandgap, high saturated electron drift velocity, and high breakdown field enable SiC a material widely used in high-temperature, high-power, high-frequency, and radiation-resistant applications.

Table 2.2: Miscellaneous properties of SiC

	3C	4H	6H
Mohs hardness	≈9 [22]	≈9 [23]	≈9 [24]
Acoustic velocity[a]	12.6 [25]	13.73 [26]	13.26 [26]
Thermal conductivity[b]	3.2 [27]	3.7 [27]	4.9 [28]
Optical bandgap[c]	2.40 [29]	3.29 [29]	3.10 [29]
Saturated electron drift velocity[d]	2.0 [30]		2.0 [30]
Breakdown field[e]	2.2 [30]		2.2 [30]

[a]Unit: ms^{-1}
[b]Unit: $Wcm^{-1}K^{-1}$
[c]Unit: eV
[d]Unit: $10^7 cms^{-1}$
[e]Unit: $10^6 Vcm^{-1}$

2.2 Fabrication Processes

2.2.1 Growth

To realize the full potential of SiC mentioned above, the most difficulty is growth of high quality and large SiC crystals without polytype mixing. Large size bulk SiCs are the key elements to realize the electronic devices, and epitaxy techniques are necessary to improve the quality of bulk material and produce complicated device structures [29] [31]. This subsection gives a review of SiC technology for bulk and epitaxy growth.

Bulk crystal growth

Physical Vapor Transport (PVT) is accomplished by the SiC transport in vapor phase from a hot sublimation source to a substrate in a cooler region of the growth furnace. It is well known that the first sublimation method was proposed by Acheson at the beginning of twentieth century and is still used today with only small modification but no fundamental changes. In Acheson method, mixture of silica, carbon, and small amount of sawdust and common salt are used to be the sublimation source. The process temperature is around 2700℃. This method yields high productivity and is widely used in SiC production for abrasive use [29]. However, the crystalline materials obtained by Achenson method are heavily contaminated due to the dirty sublimation source, and in small size with combination of different polytypes which arise

from the poorly controlled growth conditions. These drawbacks prevent its applications in electronic and semicondutor devices.

Lely proposed a method which has better crystal quality and is always free of micropipe defects [32]. In Lely method, the sublimation source is SiC powder which is placed in a porous graphite sleeve and a temperature gradient is impressed across the sleeve. The source temperature is between 2200 and 2700℃, SiC crystals are nucleated on graphite sleeve and the process could be controlled by the holes in the sleeves [33, 34]. Lely crystals have been demonstrated in device fabrication due to its high quality [35–37]. However, the crystal size is as small as in the Acheson method, and the platelet shape is irregular.

Tairov-Tsvetkov method, also known as modified or seeded Lely method, was first proposed by Tairov and Tsvetkov [38, 39]. In this method, a seed is introduced on the lid of the crucible. The source material is SiC powder, SiC polycrystalline materials, or SiC single crystals. The source temperature is between 2100 to 2400 ℃, while the growth pressure varies from $10^{-6} - 20$ torr [14, 40]. A thermal gradient around 20-35 ℃/cm is applied and the substrate is slightly colder than the powder source [40]. In SiC vapor, the principal molecular species are Si, SiC_2, and Si_2C, and the ratio between them is determined by the temperature. Growth rate of 0.5-5.0 mm/hr could be achieved [14].

High Temperature Chemical Vapour Deposition (HTCVD) has been applied in bulk SiC crystal growth and high quality crystals were obtained [41, 42]. HTCVD method uses gases instead of powder as source material, and the gases used are mainly silane, ethylene, and a helium carrier. The growth temperature is about 1650 to 1750℃, and typical growth rate of this method is about 0.8-1 mm/hr [43]. Compared with the seeded sublimation method, Si/C ratio is better controlled in HTCVD and high quality crystal is also obtained due to high purity of the gases. However, since the reactor in HTCVD is considerably more complex and hence more expensive, the manufacture cost is sometimes an obstacle for the application of this method.

Growth from liquid phase has not been widely applied in bulk SiC growth as in the other semiconductor materials. Low solubility of SiC in the Si melt limits the growth rate and inclusion incorporated in grown crystals due to parasitic phase formation [14]. However, in its later development, significant progress has been made and hence the high quality SiC crystals have been grown [29, 44–47]. Typical growth temperatures from liquid phase vary from 1900-2400 ℃, while the growth pressures

are between $7.5 \cdot 10^4 - 9.0 \cdot 10^4$ torr and growth rates are about 0.1-0.4 mm/hr [31].

Crystal size and defects are two main issues used to evaluate the quality of bulk SiC crystal. 2-inch (50 mm) to 4-inch (100 mm) silicon carbide wafers are fully commercialized at CREE, II-VI, Dow Corning and Nippon Steel. 6-inch (150 mm) has already been demonstrated since 2010 and would be in production soon, and this will definitely accelerate the cost reduction of SiC device manufacturing [48, 49]. The typical defects in SiC crystals include voids, dislocations, misoriented blocks, and foreign polytype inclusions. Defects generations were studied and defects density reduction techniques have been investigated by many works [50–59].

Epitaxial growth

Sublimation epitaxy has a lower growth temperature (1600-2100 ℃ [14]) and a slower growth rate than bulk SiC sublimation growth. However, the basic principles of these two are similar. The breakthrough of sublimation epitaxy was achieved with "sandwich method" developed by Vodakov and Mokhov [60]. In this method, a nearly flat source positioned close to the substrate and perform the growth under near equilibrium conditions, and the uncontrolled growth conditions were eliminated [61].

Chemical Vapour Deposition (CVD) is probably the main technology for SiC epitaxy growth. In this technique, gaseous compounds are transported to the substrate chamber, where chemical reaction occurs, and the SiC epitaxial layers are grown there. The typical growth temperature of CVD process varies from 1200 to 1800℃, while growth pressure varies from 100 to 760 torr [29,62]. Compared with other epitaxial techniques, CVD has the adavantages in precise control and uniformity of epitaxial layer thickness and inpurity doping [15]. Homoepitaxial growth of SiC have also been achieved by using step-controlled epitaxy with off-oriented SiC substrate [63, 64]. And a growth rate of 2 μm/hr has been reported [15].

Liquid Phase Epitaxial (LPE) is a crystallisation from supersaturated solution of Si and C in a melt solvent. The most common melt for SiC LPE is silicon, while other materials such as Sn, Ge, Ga and their alloy are also used [29]. The growing layers are in equilibrium with the liquid phase and the growth takes place at temperatures of 1200-1700℃ [65]. Typical growth rate varies from 0.5-10 μm/hr. For traditional LPE, disadvantges such as difficult to control the surface

morphology limit its applicaiton, however, new achievement makes it as a good alternative for micropipe closing and heavily doped p-type film growth [14, 65].

Different growth techniques were briefly introduced here. So far, CVD is the only technique in commercial SiC growth. However, efforts are keeping making on other process techniques and material performance of them become more competitive.

2.2.2 Doping

SiC can be doped by several substitutional impurities. Most common donor impurities (n-type) are nitrogen, and to some extent phosphorus, whereas aluminum and boron are the most common ones as acceptors (p-type). The doping technolgy in SiC shows the dependence on surface orientation, doping technology, doping concentration, and also polytype structure. Impurities diffusion and ion implantation are the two principal methods of doping.

For impurities diffusion, it is found that the solubility of impurities in 6H-SiC have a crystal face dependence because of the strong orientation doping anisotropy of 6H-SiC. In addition, it appears that the solubility of impurities and their diffusive mobilities in different SiC polytype are very similar [29]. However, due to the very high bond strength possessed by SiC, the effective diffusion coefficients for most of the major impurities in SiC are too small for standard device processing (temparature lower than 1800 ℃) [17].

Ion implantation is the only suitable alternative to realize doping during growth and is of great importance in doping technology of SiC device fabrication. N-type doping by ion implantation has been developed into a production process. On the other hand, due to relatively deep ionization energy of both aluminum and boron atoms, device-quality p-type doping is difficult to realize since a higher annealing temperature and longer time are required to complete ionization. Good review work on the behaviour of different ion species implanted in SiC and recent technology progress have been producted by Harris [29] and Saddow [43].

2.2.3 Etching

As a highly refractory material, SiC could be chemically etched only by a few hot gases (chlorine, hydrogen) and hot molten salt (NaOH, KOH, etc.) [66]. However, chemical etching is impractical for device fabrication

since high temparature is requird and conventional photoresist, oxide, and metal masks are not usable at that temparature [29].

As alternatives, two types of vacuum plasma etching techniques are widely used in SiC fabrication which are plasma etching and reactive ion etching (RIE). Plasma etching use RF energy to generate plasmas by dissociating the active gases, and plasmas are chemically reacted with C and Si and then generate the volatile products. CF_4 and SF_6 gases are commonly used as plasmas source. It is reported that CF_4 plasma produce a surface layer which would limit the etching rate [67] and SF_6 does not have this limitation and hence has faster etching rate [68].

RIE is similar to the plasma etching and usually use fluorinated gases to etch SiC. However, RIE also includes physical removal of C and Si atoms by sputtering, and the removal occurs by the following reaction mechanism in Eq. 2.1 [69].

$$\begin{aligned} CF_4 + O_2 &= CF_x + F + O + (CO, CO_2) \\ SF_6 &= S + 6F \\ SF_6 + O_2 &= S + 6F + 2O \\ Si + 4F &= SiF_4 \\ C + xF &= CF_x \\ C + xO &= CO, CO_2 \end{aligned} \tag{2.1}$$

RIE has faster etch rate than plasma etching and highest rate of 2000 $\text{Å}min^{-1}$ could be obtained [29].

Photoelectrochemical (PEC) etching is a relatively new technique. It uses ultraviolet light, voltage, and chemicals to etch n-type SiC. Through PEC etching, holes are generated with ultraviolet light by breaking some of the bonds in the SiC, then voltage is applied to the sample forcing holes to the surface of the sample to facilitate etching by hydrofluoric acid. This procedure could be explained by the following chemical reactions suggested by Lauermann in Eq. 2.2 [70].

$$\begin{aligned} SiC + 4H_2O + 8h^+ &\rightarrow SiO_2 + CO_2 + 8H^+ \\ SiC + 2H_2O + 4h^+ &\rightarrow SiO + CO + 4H^+ \end{aligned} \tag{2.2}$$

The oxides (SiO_x, CO_x) are removed from the surface by HF dissolution and gas phase nucleation respectively. Main advantages of PEC etching to the RIE are higer etching rate, high dopant selectivity, and less surface damage. However, the disadvantage is that an ohmic contact

is required on the SiC to proceed electrochemical etching which add an additional processing step.

2.3 Applications in LEDs

In 1907, Round observed light emission from a solid-state materials (SiC), caused by an electrical pumping. This phenomenon was termed as electroluminescence and it is the very first time Light-Emitting Diode (LED) invented [71]. The electroluminescence can occur at room temperature, and it is fundamentally different from incandescence, which is the visible electromagnetic radiation emitted by a material heated to high temperatures, typically > 750 °C. In 1960s, three research groups (General Electric Corporation, MIT Lincoln Laboratories, and IBM Corporation) produced the first viable LEDs. LEDs have become devices in their own right and today possibly are the most versatile light sources available to humankind [8].

During the last five decades, technical progress in the field of LEDs has been breathtaking, and the efficiency and reliability of LEDs have been dramatically improved. Owing to the merits of small, rugged, reliable, bright, efficient and wide emission spectral range, LEDs are widely used in many applications, including displays, short-distance communications over fibers, opto-isolators (optocouplers), indicator lights, high-brightness lamps, and infrared wireless communication. LEDs also enter new areas such as medical operation, automotive headlights, and even the domain of arts [8,72–75]. Today LEDs are being extensively used in general illumination applications and challenging Edison-style incandescent lamps [76]. The peak efficiency of white LEDs exceeds 300 lumens per watt (lm/W), compared with around 16 lm/W for incandescent lamps and less than 100 lm/W for fluorescent lamps. The performances are still growing. Meanwhile, SiC plays different roles in the progress of LEDs technology, nevertheless, it can be classified into two main groups where SiC plays as active structure and substrate respectively.

2.3.1 SiC as active structure

As a result of wide bandgap (3.101 eV for 6H-SiC and 3.285 for of 4H-SiC), SiC can be tailored to emit light across the entire visible spectrum, as well as the near UV. Although its indirect bandgap makes light emission relatively inefficient, many scientifically interesting and

Table 2.3: Ionization energy (meV) of impurities in common SiC polytypes [29,77,78]

Polytype	E_g [a]	Nitrogen	Aluminium	Boron
3C	2403	56.5	254	735
4H	3285	h[b]: 66, k[c]: 124	191	647
6H	3101	h: 100, k: 155	h: 239, k: 249	h: 698, k: 723
15R	2946	h: 64, k: 112 k: 223, 230, 236	h: 206, 221	h: 666, k: 700

[a] Energy bandgap: meV
[b] hexagonal site
[c] cubic site

commercially successful LED devices have been developed [14].

Different dopants are usually introduced during the fabrication of SiC, as a result, the emission wavelength is determined by the optical bandgap of certain polytype structure and the impurity levels in it. In different polytype structure, various combinations of inequivalent sites are exist and these inequivalent sites are expected to cause site-dependent impurity levels which are summarized in table 2.3.

SiC green LEDs

The green LED was demonstrated by implanting aluminum into an n-type 6H-SiC epilayer of 10 to 30 μm thick and grown by sublimation epitaxy [79]. The Al implant produced the p-type region of the p-n junction, and the injection-luminescence mechanism of this type of LED is associated with stable nonequilibrium point defects (D_1 centers) that were simultaneously generated during the growth process and also when the SiC is bombarded by high-energy particles [61]. The resulting LEDs emitted the green light with peak wavelength of 530 nm and bandwidth of 85 nm. The output power is in the range of 5 to 15 μW, and the highest external quantum efficiency (η_{ext}) of 0.4 % had been obtained at 1 mA forward current.

Besides, another type of green SiC-LED was demonstrated by Barash [80]. The 4H-SiC heteroepitaxial layer was grown by a sublimation sandwich method in the presence of a group IV impurity (Ge, Sn, Pb), Boron was introduced by diffusion, and the substrates were n-type 6H-SiC or n-type 15R-SiC grown by Lely method. Green illumination colors (520-530 nm) arise from the recombination at nitrogen-boron donor-acceptor-

pairs (DAPs) was obtained.

SiC blue LEDs

Blue LEDs based on 6H-SiC emitting in the spectral range from 460 to 480 nm were fabricated by LPE [81, 82] and by CVD epitaxy [83]. The highest η_{ext} reported was achieved by Hoffmann [82] at Siemens Research Laboratory. By using a high-resistivity transparent p-type substrate with contacts made to via-etched topsided p^+ and light-emitting compensated n-type epilayers, deposited via LPE, maximum η_{ext} of 0.02 % was exhibited. However, the typical commercial devices with a vertical device configuration had much lower value of 0.004 % with excessive forward voltage (4-8 V) due to low optical transparency and high electrical resistivity of the p-type substrate employed [14].

Cree Research produces the only commercially available SiC blue LED today of which epitaxial growth is achieved via CVD [83, 84]. This device emits light with a peak wavelength of 470 nm and a spectral halfwidth of 70 nm. The optical output power is 34 μW at a forward current of 20 mA, and this represents an η_{ext} of 0.07 %. The injection-luminescence mechanism of Cree's LED device is associated with phonon assisted donor-acceptor pairs recombination between nitrogen donors and aluminum acceptors, as well as with radiative recombination of the band-impurity type.

In addition, another type of blue LED was also obtained based on aluminum implanted 4H-SiC junctions, where the luminescence is attributed to the stable nonequilibrium point defects (D_1 centers) [85].

SiC LEDs in other color

A 6H-SiC LED emitting in violet-blue region of spectrum (425 nm) was observed visually at room temperature [86]. A container-free version of LPE is used and the substrate is 6H-SiC single crystal grown by the Lely method. The recombination type is radiative recombination of free excitons.

Dmitriev [87] demonstrated a SiC violet LED device which had the p-n structure with an n-type 4H-SiC substrate containing nitrogen donors and an epitaxial p-type 4H-SiC film grown by container-free LPE and doped with aluminium acceptors. The η_{ext} was about 0.005 % at room temperature and it decreased with increased temperature. The maximum of the luminescence spectrum was located at 423 nm.

Table 2.4: Comparison of common substrates for GaN growth

	Sapphire	SiC	Si
Lattice mismatch (%)	16	3.5	18
Thermal conductivity (W/Kcm)	0.46	4.9	1.5
Thermal expansion coefficent (10^{-6}/K)	1.9	-1.1	5-20
Dislocation density (cm^{-2})	10^{10}	10^{8}	
Surface roughness (nm RMS)	0.1	1	

LEDs with red and yellow electroluminescence could be fabricated from beryllium-nitrogen co-doped 6H-SiC and diffusion of boron in 6H-SiC epitaxial layers [88, 89].

2.3.2 SiC as substrate

Based on various polytypes of SiC, LEDs have been created to emit lights covering the visible spectrum. Both green and blue (relatively successful) SiC LEDs have been developed commercially in 1990s. However, their efficiency and brightness is far below that of group III-V-based green and blue LEDs produced by Cree, Nichia and others [14], due to its indirect bandgap property. As a result, SiC could no longer compete with III-V semiconductors as active structure in LEDs. However, 6H-SiC has been proved to be an excellent substrate for heteroepitaxial growth of III-nitrides LEDs [84].

To date, high efficiency blue and green LED emission has been achieved by employing the direct bandgap alloy system AlN-InN-GaN, which has a chemical and structutal compatibility with SiC substrate. Table 2.4 summarized some optical properties of three commonly used substrates for GaN growth. Compared with sapphire which is mostly used as substrate presently, SiC has two major merits. Firstly, it has a lattice mismatch of 3.5% with GaN, in relative to sapphire's 16% which results in a dislocation density of 10^{10} cm^{-2}. Secondly, SiC could be conductive, which allows for the fabrication of a vertical device structure for nitride-based LED device. While in sapphire-substrate device, it needs two topside contacts to pass the current through the p-n junction due to the electrical insulation of sapphire [14]. In addition, SiC also has a better thermal conductivity which is preferred in high power LED applications.

The application of SiC as substrate in LEDs fabrication is growing

rapidly. Although the price of SiC substrate is still realtively high compared with sapphire substate, some manufacturers like Cree has already been using 6H-SiC substrates for commercial production of nitride-based LEDs.

2.4 Summary

SiC are reviewed as a material from its crystal structures, various properties, to fabrication process. Its applications in LEDs are also described, where its role is changing from the active structure in the early stage to the present substrate material. It is believed that with improving fabrication techniques, full potential of SiC will be explored and widely used in semicondutor electronics and optoelectronics applications.

Chapter 3

Fluorescent silicon carbide

3.1 Donor-acceptor-pair emission

To explore how N and B doping concentrations affect Donor-Acceptor-Pair (DAP) emission, five homoepitaxial layers of 6H-SiC with different doping concentrations were grown by Fast Sublimation Growth Process [90]. The growth process is driven by a temperature gradient created between the source, in a form of polycrystalline SiC plate, and the substrate. Boron was introduced into the epilayers by doping from the source and nitrogen incorporation was controlled by adjusting N_2 gas pressure during the growth. Epilayers with different concentrations of B and N were grown on 6H-SiC (0001) substrates with 1.4 degree off-orientation in the $[11\bar{2}0]$ direction at the growth temperature of 1725°C. Atomic dopant concentrations of the epilayers measured by Secondary Ion Mass Spectrometry (SIMS) are listed in Table 3.1, where N_A and N_D represent acceptor (B) and donor (N) concentrations respectively.

Photoluminescence (PL) measurements were realized by using a diode laser working at 377 nm as excitation source which was coupled to a reflected fluorescence microscope (shown in Fig. 3.1). The excitation

Table 3.1: Boron (N_A) and nitrogen (N_D) concentrations of sample a to e.

	a	b	c	d	e
N_A (10^{18} cm^{-3})	8.0	6.9	6.9	4.4	5.2
N_D (10^{18} cm^{-3})	0.04	3.2	6.0	9.0	9.2
Conductive type	p	p	p	n	n

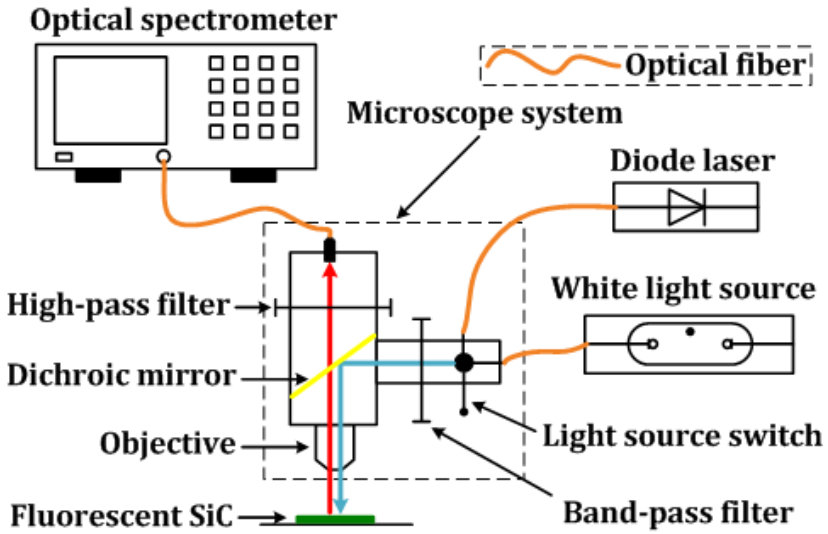

Figure 3.1: Schematic diagram of photoluminescence and reflectance measurement setup based on a microscope system.

power density was 0.02 W/cm^2, and the measurements were performed at room temperature. The PL spectra were acquired by an optical spectrometer (Instrument Systems CAS140S) and are shown in Fig. 3.2. One can see that the high-level p-type sample (a) exhibits extremely low DAP emission intensity, while the low-level p-type samples (b, c) have relatively stronger DAP emissions but still at a low level. Intense DAP emission was observed in n-type samples (d, e) while the strongest DAP emission occurred in sample d with the largest concentration difference of 4.6x10^{18} cm^{-3}.

Despite the intensity differences, all the DAP emission spectra show the same peak wavelength at 587 nm (2.12 eV) and the same Full Width at Half Maximum (FWHM) of 120 nm. The spectrum shape of the DAP emission is usually determined by the coulomb interaction and phonon coupling rather than by the carrier populations [93,94]. Due to the same dopant materials and experimental conditions, the FWHM is almost constant for all the fluorescent samples. From the above results, it is clear that both the doping type and the concentration difference affect the DAP emission intensity but do not introduce a change in the peak wavelength and FWHM at this doping level.

The dependence of the DAP emission intensity on doping concen-

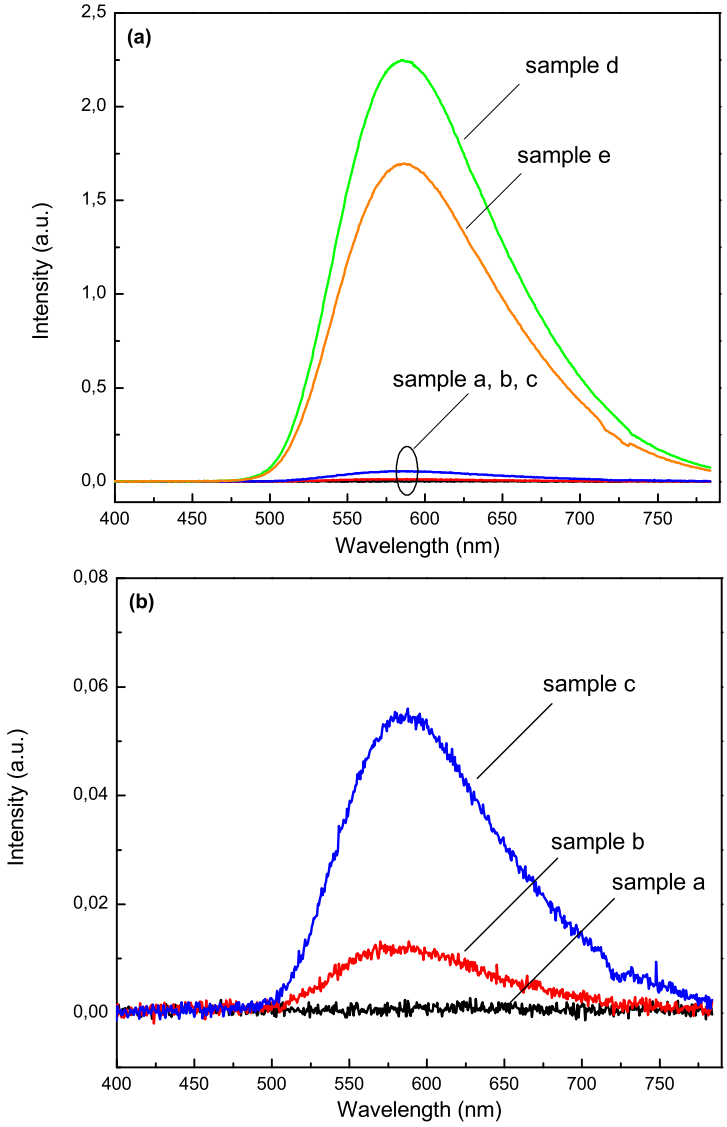

Figure 3.2: (a) Measured PL spectra for sample a-e, and (b) zoom-in for sample a-c.

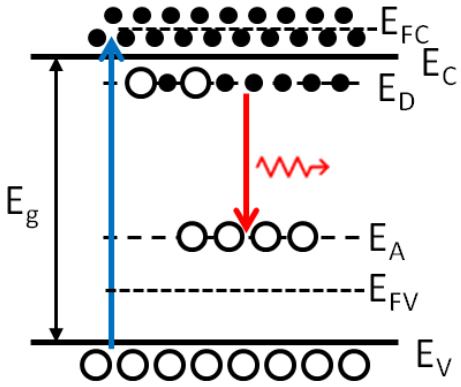

Figure 3.3: Band diagram of n-type SiC under excitation (black dots represent electrons and unfilled circles represent holes; electron and hole quasi-Fermi levels are represented by E_{FC} and E_{FV} respectively. $E_D \approx 0.17$ eV [91], $E_A \approx 0.72$ eV [77], and $E_g \approx 3.02$ eV [92]).

trations could be explained by using band diagram with Fermi-Dirac statistics. Fig. 3.3 shows a schematic band diagram of n-type doped SiC under excitation condition. It is seen that all the acceptor states (E_A) are occupied by photo-excited holes due to the large ionization energy of acceptor states (E_A-E_V), so the hole density at the acceptor states $p_A \cong N_A$. On the other hand, the electron density at donor states (E_D) under excitation is given by

$$n_D = N_D \cdot F_D \tag{3.1}$$

due to the small ionization energy (E_C-E_D). Here F_D is the occupancy probability of an electron on donor states. It can be represented by

$$F_D = \frac{1}{1 + \frac{1}{2} exp\left(\frac{E_D - E_{FC}}{kT}\right)} \tag{3.2}$$

where E_{FC} is the electron quasi-Fermi level under excitation, k is the Boltzmann constant, and T is the absolute temperature.

The DAP recombination rate R_{DA} is proportional to the product of p_A and n_D, hence,

$$R_{DA} \propto N_D \cdot F_D \cdot N_A \tag{3.3}$$

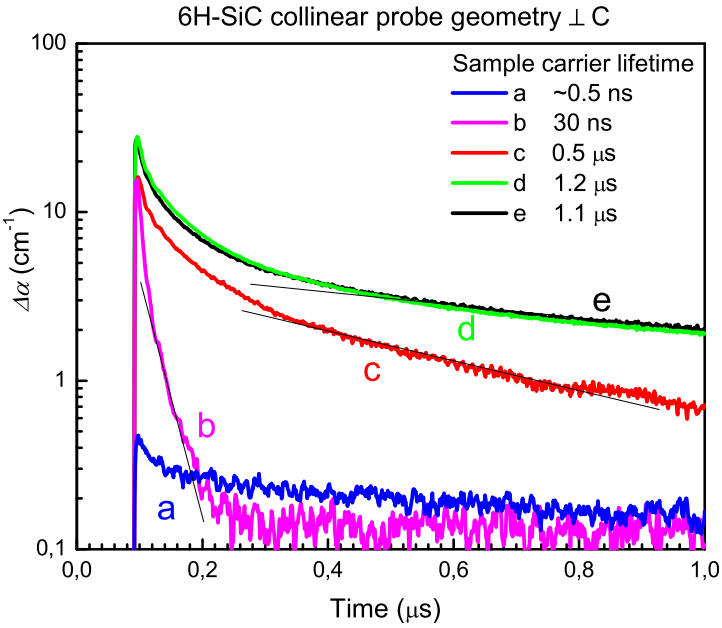

Figure 3.4: Induced free carrier transients in different 6H-SiC epilayers at constant excitation by 355 nm 2 ns laser pulses. Carrier lifetime in the sample a is shorter than duration of the laser pulse, this produces a large drop of the induced absorption amplitude.

Large donor and acceptor doping concentrations are required to achieve intense DAP recombination according to Eq. 3.3. In addition, the n-type sample is more likely to achieve high electron density at donor states. That is because, E_{FC} is at a higher energy level in the n-type samples than in the p-type ones. When N_A of the samples are in the same level and the concentration difference $(N_D - N_A)$ increases, E_{FC} becomes larger and could be within the conduction band. As a result, F_D increases and a high electron density could be generated at donor states. This is in good accordance with our PL measurement results.

Carrier lifetime measurements of the samples were carried out by using 355 nm, 2 ns, 40 Hz laser pulses in the work [95]. The obtained carrier lifetimes from sample a to e are 0.5 ns, 30 ns, 0.5 μs, 1.2 μs, and 1.1 μs respectively and the results are shown in Fig. 3.4. Combined with PL results, it is found that the longer carrier lifetime is responsible for stronger emission intensity. Sample d with the largest concentration difference of $N_D - N_A$ has the longest carrier lifetime of 1.2 μs, which

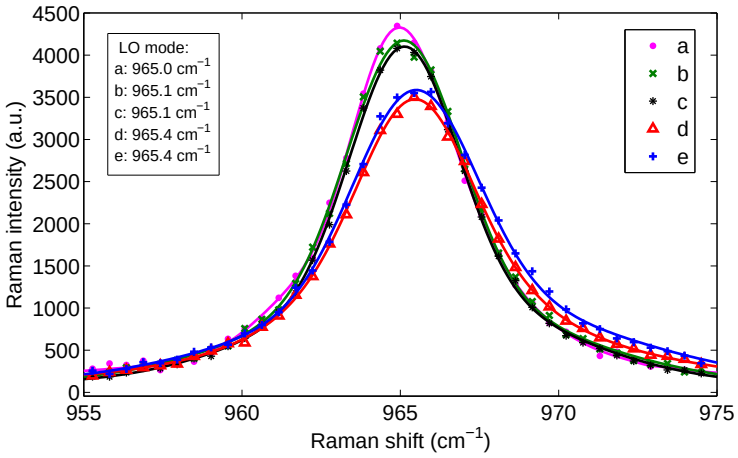

Figure 3.5: LO mode of the Raman spectra (inset: positions of LO modes; peak height decreases in the order of a, b, c, e, d).

is comparable to the values of common phosphors: 0.89 μs in Ref. [96] and 1.4 μs in Ref. [97].

However, very high $N_D - N_A$ will cause intra-band absorption of excitation light and severe Auger recombination, both of which reduce the emission efficiency. So optimal concentrations need to be further studied.

3.2 Raman spectroscopy

Raman scattering spectra of the 6H-SiC samples were acquired in a backscattering configuration using the 514.5 nm line from an Ar ion laser (5 mW). Longitudinal Optical (LO) modes of the Raman spectra are shown in Fig. 3.5, and the mechanisms of the observed Raman shifts in p- and n-type samples are different.

In p-type samples, very few acceptor states are ionized due to the large ionization energy, and the Raman shift is mainly attributed to the atomic size effect [98]. Boron atoms usually are believed to occupy Si lattice positions in SiC. The interatomic distance of a Si-C bond is longer than that of a B-C bond due to the smaller atomic radius of B. The biaxial tensile stress will be released which results in a decrease of the phonon oscillation frequency. So the LO mode shifts toward smaller wavenumbers with higher B concentrations.

In n-type samples, the predominant mechanism causing the Raman shift of the LO mode is the coupling interaction between LO phonons and overdamped plasmons [99, 100].

The plasmon frequency ω_P is given by

$$\omega_P = \sqrt{\frac{4\pi n e^2}{\epsilon_\infty m^*}}, \tag{3.4}$$

where n, e, ϵ_∞, and m^* are the free carrier concentration, electron charge, optical dielectric constant, and effective mass of electron respectively. The LO mode is then redefined as Longitudinal Optical Plasmon Coupled (LOPC) mode.

From Eq. 3.4, it is seen that ω_P is proportional to $\sqrt{n}$. So the plasmon frequency increases with increasing the free electron concentration, which results in an enhancement of the coupling interaction between phonons and plasmons. Consequently, the LOPC mode would lower its intensity and shift toward higher wavenumbers. Usually, the LOPC mode is more sensitive to the presence of free electrons than to the free holes. This is in a good agreement with the results shown in Fig. 3.5, where the LOPC modes of n-type samples occur at significantly higher wavenumbers than the p-type ones. Although no obvious peak shift has been observed between sample d and e due to the relatively small concentration difference, the peak intensity of the LOPC mode decreases as expected when the free electron concentration $(N_D - N_A)$ increases from sample e to d.

3.3 Angle-resolved photoluminescence

Angle-Resolved Photoluminescence (ARPL) was measured on sample d by using a goniometer system (Instrument Systems GON360) which illustrated in Fig. 3.6. The excitation light was fixed to a certain direction, and the observation (emission) angle varied from 0 (normal to the sample surface) to 80°. From the acquired spectra shown in Fig. 3.7a, one can see that the PL intensity decreases and its peak shifts toward shorter wavelength as the emission angle θ increases.

The PL intensity becomes lower because the internal reflection increases as the emission angle increases, hence, the emission light extracted out of the SiC sample decreases. From Fig. 3.7b, it is also seen that the luminescence intensity at an angle of 80° is still around 57 %

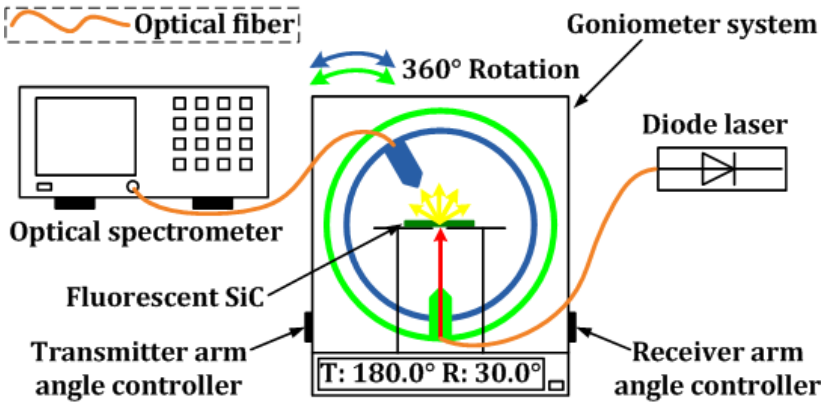

Figure 3.6: Schematic diagram of ARPL measurement setup based on a goniometer system.

of the one normal to the surface, which is quite promising among the most of commercial LEDs (less than 30 %). In addition, this angular-dependent PL peak wavelength is attributed to the Fabry-Pérot micro-cavity interference effect, and similar phenomena have also been observed in Refs. [101, 102].

The Fabry-Pérot equation

$$m\lambda = 2dn\cos\psi. \tag{3.5}$$

gives the condition for constructive interference of light undergoing multiple internal reflections in a solid film or an étalon like illustrated in Fig. 3.8. In Eq. 3.5, m is the interference order, λ is the propagating wavelength, d is the étalon thickness, n is the refractive index of the étalon, and ψ is the wave-front propagation angle with respect to the surface normal. The relationship between ψ and θ can be represented by Snell's law

$$n\sin\psi = \sin\theta. \tag{3.6}$$

Thus, the Fabry-Pérot equation can be rewritten as

$$m\lambda = 2d\sqrt{n^2 - \sin^2\theta}. \tag{3.7}$$

The N-B doped SiC film grown on the 6H-SiC substrate has a large refractive index difference at the SiC-air interface. Also due to its smooth surface, it acts as a Fabry-Pérot étalon and thus optical interference occurs. The DAP emission in SiC is broad as shown in the PL spectra. From Eq. 3.7, it is clear that the interference wavelength decreases

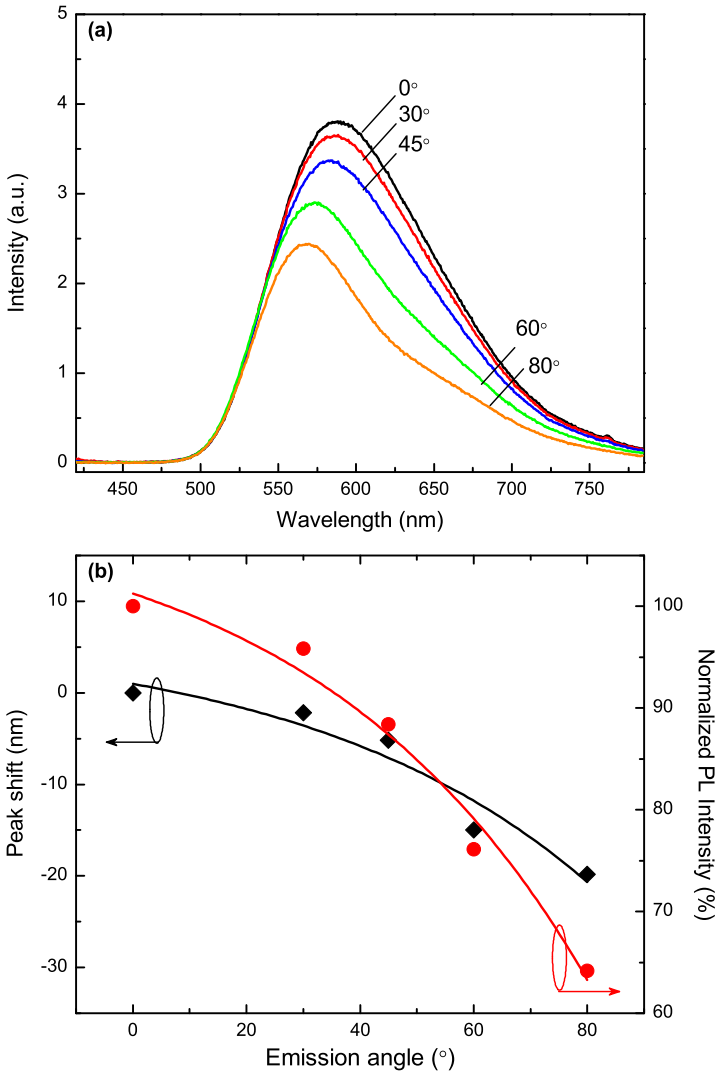

Figure 3.7: (a) Angular-dependent PL spectra; (b) emission angle versus peak shift and normalized PL intensity (%).

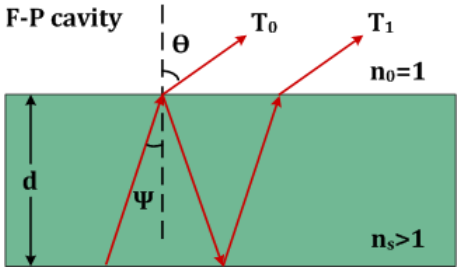

Figure 3.8: Schematic view of a Fabry-Pérot cavity.

as θ increases. The PL peak shifts toward shorter wavelengths as the emission angle increases and this is consistent with the observed results.

However, for the illumination application, the light source should not depend on the emission angle in terms of the peak wavelength. To improve it, nanostructuring of the surface to remove the Fabry-Pérot interference and increase the luminescence intensity at large emission angle should be interesting to study for a comparison.

3.4 Summary

In conclusion, five fluorescent SiC samples with varied B and N doping concentrations were investigated. It is found that n-type doping with both B and N concentrations larger than 10^{18} cm^{-3} is required to achieve intense DAP emission, and the concentration difference of the n-type sample needs to be larger than 4x10^{18} cm^{-3} as concluded from this study. The doping type and concentrations of the samples were then confirmed by analyzing the LO mode variation in Raman spectra.

The luminescence intensity at an emission angle of 80° is found to be 57 % of the one normal to the surface. Angular-dependent PL spectra which arised from the Fabry-Pérot microcavity interference effect was also observed and expected to be removed by applying surface nanostructuring. With adjustment of doping concentrations, intense DAP emission with a broad spectral range was obtained making fluorescent SiC a good candidate of wavelength-conversion material in white LEDs.

Chapter 4

Modelling of antireflective subwavelength structures

4.1 Surface antireflection and colorimetry

It is well known that the efficiency of Light-Emitting Diode (LED) is determined by the product of the internal quantum efficiency and light extraction efficiency. Extremely high internal quantum efficiency could be achieved, however, the light extraction efficiency is usually low due to the internal reflection loss arising from large refractive index difference between semiconducor materials and air interfaces. As a result, enhancement of the light extraction efficiency becomes especially important in LEDs applications.

Various approaches have been proposed to enhance the light extraction efficiency of LEDs during the last decades. Fig. 4.1 shows the schematic diagram of semiconductor substrate with enhanced light trasmittance by using different methods. Traditionally, a single-layer quarter-wavelength thin-film antireflection coating can be applied to enhance the lighting for a specific wavelength at very low level (Fig. 4.1b). Broadband application can be achieved by applying a stack of antireflection coatings with appropriate design (Fig. 4.1c) [103, 104], however, it is usually limited by the availability of materials with suitable refractive indices and thermal expansion coefficients [105]. Depositing quarter-wavelength coatings also requires high vacuum conditions, therefore adding extra cost to the fabrication processes. Meanwhile, methods relying on random light redirecting such as surface roughening have been employed [106, 107], and increasing research effort have been

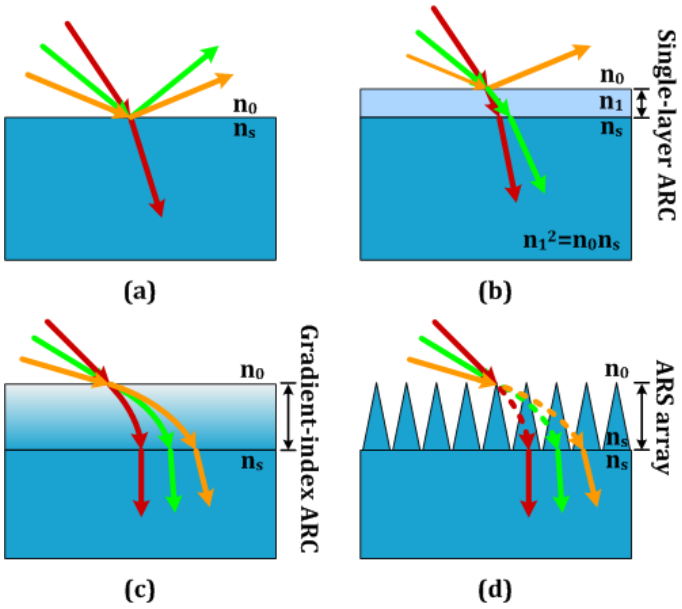

Figure 4.1: Schematic diagram of semiconductor substrate with (a) bare surface; (b) single-layer quarter-wavelength antireflection coating; (c) gradient-index antireflection coating; and (d) antireflective subwavelength structures.

intensively devoted to the Antireflective Structures (ARS) (Fig. 4.1d) such as photonic crystal [108–112], nanopillar [113–116], and nanocone structures [105, 117, 118]. Among all of these methods, ARS have been considered as an effective method to enhance the light transmittance over a broad spectral bandwidth.

Besides the high quantum efficiency, an excellent light quality is also desired for white LEDs. To quantify the sensation caused by different color, the International Commission for Illumination (CIE) has standardized the measurement of color by means of color-matching functions and the chromaticity diagram (CIE, 1931). The (x, y) chromaticity diagram is shown in Fig. 4.2. Reddish and greenish colors are found for large values of x and y, respectively. Bluish colors are found for low values of x and y. White light consists of numbers of monochromatic colors. To characterize the white light, Planckian black-body radiation spectrum is used as a useful standard which could be described by only one parameter, namely Color Temperature (CT). The location of Planckian locus on the CIE 1931 (x, y) chromaticity diagram is also shown in Fig. 4.2. The color temperature of a white light source , given

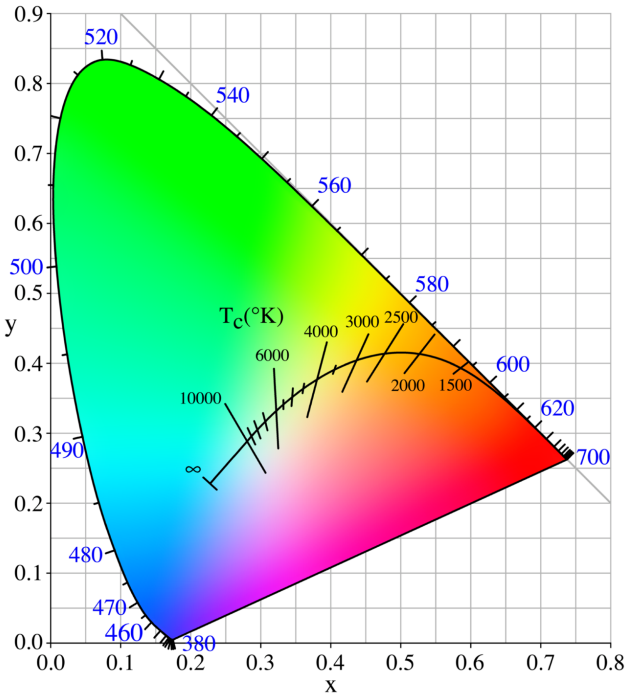

Figure 4.2: CIE 1931 (x, y) chromaticity diagram showing Planckian locus, monochromatic colors are located on the perimeter and white light is located in the center of the diagram.

in units of kelvin (K), is the temperature of a planckian black-body radiator that has the same chromaticity location as the white light source considered. With increasing color temperature, the black-body radiator glows in the red, orange, yellowish white, white, and ultimately bluish white. If the color of a white light source does not fall on the planckian locus, the Correlated Color Temperature (CCT) given in units of kelvin is then used. The correlated color temperature of a white light source is defined as the temperature of a planckian black-body radiator whose color is closest to the color of the white light source.

The Color Rendering Index (CRI), is a quantitative measure of the ability of a light source to reproduce the colors of various objects faithfully in comparison with an ideal or natural light source (reference source). A reference source, such as black body radiation, is defined as having a CRI of 100. This is why incandescent lamps have that rating, as they are, in effect, almost black body radiators. The best pos-

sible faithfulness to a reference is specified by a CRI of 100, while the very poorest is specified by a CRI of 0. A high CRI by itself does not imply a good rendition of color, because the reference itself may have an imbalanced spectral power distribution if it has an extreme color temperature. A CRI between 90 and 100 is suitable for virtually all illumination applications. A CRI between 70 and 90 is uitable for many standard illumination applications. Light sources with a CRI below 70 are considered to be of low quality.

In this chapter, we theoretically investigated how ARS affect the colorimetry of Fluorescent Silicon Carbide (f-SiC) based white LED in terms of CRI and CCT. Meanwhile, the impact of ARS on light extraction enhancement of fluorescent SiC has also been systematically examined.

4.2 Impact of ARS on white light colorimetry

To investigated how ARS affect the white light spectrum generated by fluorescent SiC based white LED in respects of the CRI, CCT, and light extraction efficiency. Applying both cylinder and cone structures on fluorescent SiC surface have been studied in the simulation based on the rigorous coupled wave analysis algorithm [119].

The simulation is based on the two dimensional Rigorous Coupled-Wave Analysis (RCWA) algorithm, and both cone and cylinder structures are arranged in the hexagonal grid. In the simulation of cone structure, the structure array is approximated by a stack of 100 horizontal layers with increasing radii from air to the substrate. The reflectance of the whole system is obtained by solving the Maxwell equation in each layer and matching the electromagnetic boundary conditions between neighboring layers from the RCWA calculations. Meanwhile, the cylinder structure array has been considered as a single layer with certain refractive index and radius in the simulation. In both structures, the grating period is defined as p and is the distance between the centers of the neighboring structures, d is the width of the structure, and h is the height of the structure (illustrated in Fig. 4.3). Since structure width has a relatively weak influence on the light transmittance [105, 117, 120], fixed values of d=120 nm and p=1.4d have been applied as optimized profile in all the following simulations. The working wavelengths were set from 360 nm to 800 nm to cover the whole visible light range. Based on the validity confirmation, normal light incidence to the surface was

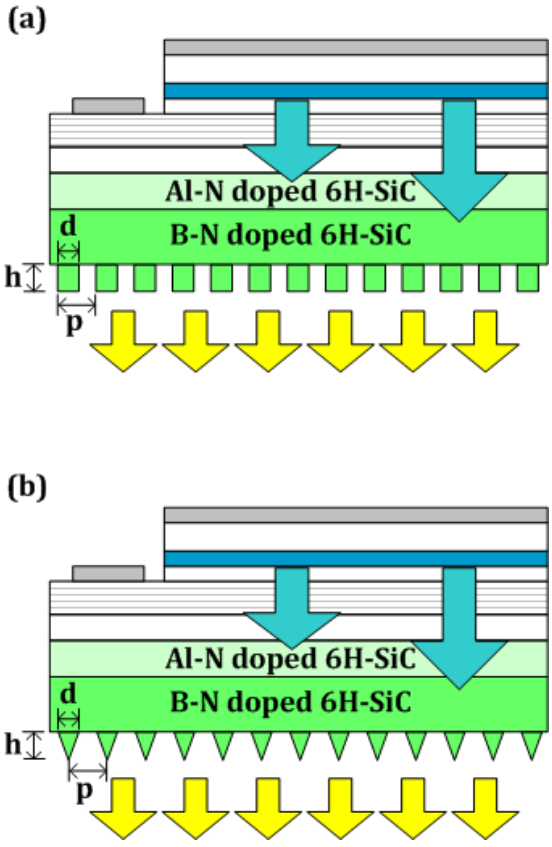

Figure 4.3: Schematic cross-section of modeled monolithic white LED (a) with cylinder structure, (b) with cone structure.

applied for the simplification. The structure height varied from 0 to 800 nm in steps of 5 nm.

According to the preliminary experimental results, the B-N doped SiC layer could produce a broad Donor-Acceptor-Pair (DAP) luminescence peaked at 580 nm with a Full Width at Half Maximum (FWHM) of 120 nm. In addition, the Al-N doped SiC layer could also produce a broad DAP luminescence with similar FWHM but the peak wavelength varies between 420 and 460 nm depending on the doping level. We first simulated these two luminescence peaks with best fit to the experimental results (1.5 and 1 order Gaussian profile for Al-N and B-N DAP luminescenece respectively). Its combination has a maximal CRI of 92.68 with a CCT of 9610 K (see Fig. 4.4), and its distance to the Planckian

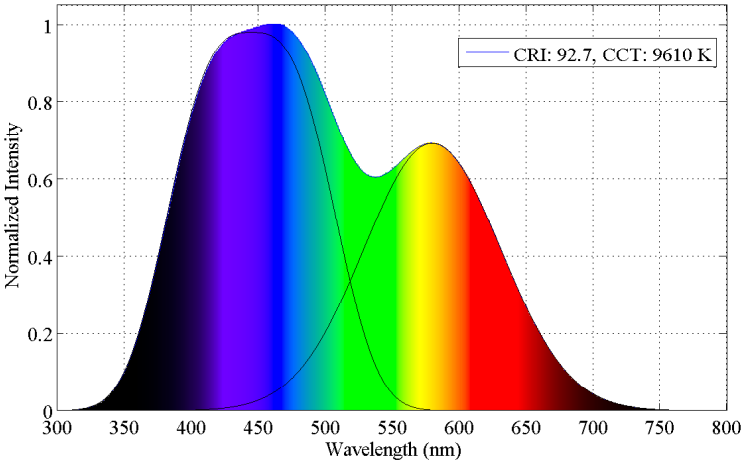

Figure 4.4: Simulated spectrum with two peaks for Al-N emission and B-N emission respectively. The Al-N emission is simulated as a 1.5 order Gaussian distribution and B-N emission is simulated as a standard Gaussian distribution.

locus in the chromaticity diagram is only 2.72×10^{-3}.

The final transmitted spectrum is achieved by the product of the simulated spectrum and the transmittance curves. By changing the structure type and varing the structure height, different transmittance curves could be obtained, thus the variation of CRI, CCT, distance to the Planckian locus, and the integrated intensity over the entire visible light range of the final transmitted spectra could be calculated. All these results have been shown in Fig. 4.5. From Fig. 4.5a, it is found that cylinder structure could affect the CRI in the range of $\pm$ 1.2 while cone structure only affect the CRI in the range of $\pm$ 0.2. The highest CRI value which closes to 94 was achieved in a cylinder structure. Similar phenomenon has also been observed in Fig. 4.5b. With the same structure height, cylinder structure could affect the CCT value much more dramatically than the cone structure. In general, any point in the chromaticity diagram whose distance to the Planckian locus is within 5.4×10^{-3} is defined as "white color". According to this definition, almost all the transmitted spetra of both structure types are located in the "white area" in the chromaticity diagram only except a few examples for the cylinder structure (see Fig. 4.5c). The integrated intensities of the transmitted spectra over the entire visible range for both structure types have been calculated and results are shown in Fig. 4.5d. All the

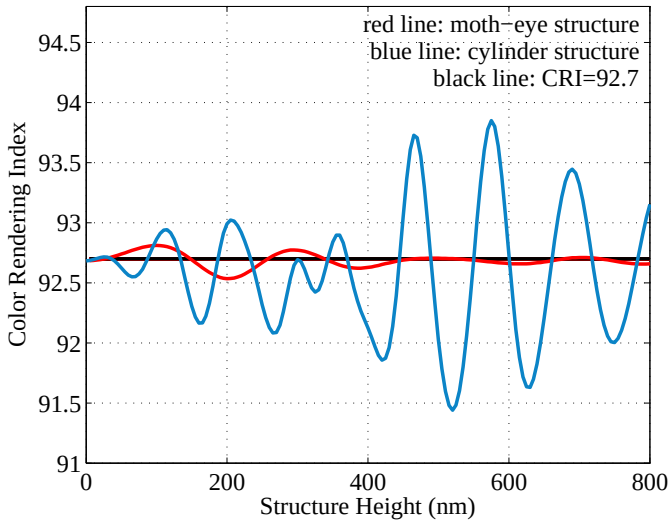

(a)

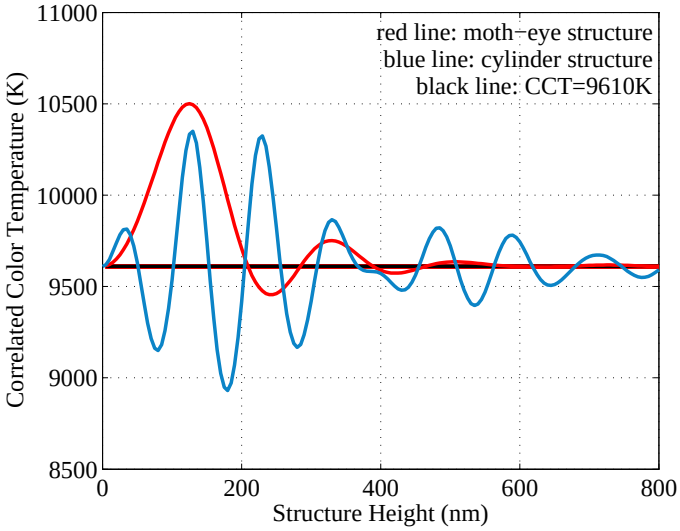

(b)

Figure 4.5: (a) CRI, (b) CCT of cylinder (blue line) and cone structures (red line) as functions of the structure height.

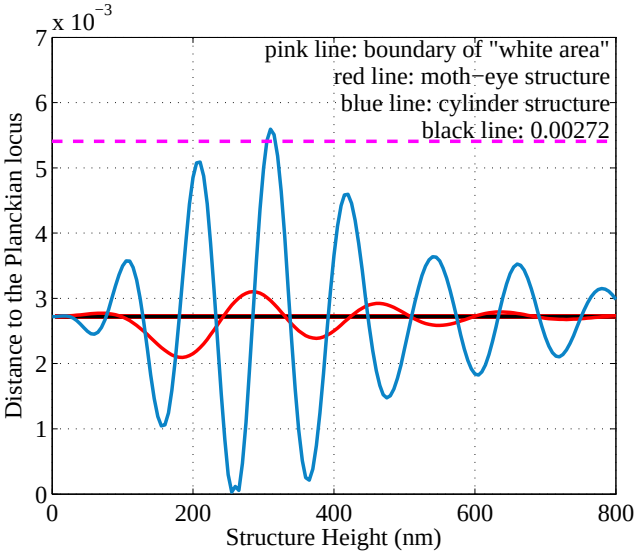

(c)

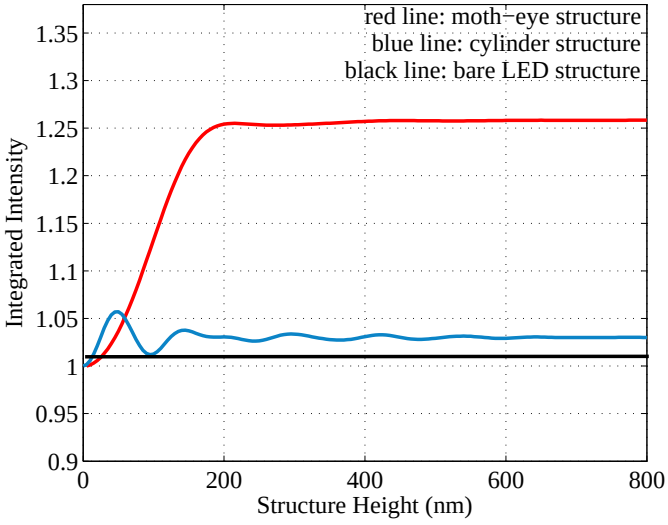

(d)

Figure 4.5: (c) distance to the Planckian locus, and (d) integrated intensity of cylinder (blue line) and cone structures (red line) as functions of the structure height.

Table 4.1: Comparision of three examples: (a) none structure, (b) highest CRI (cylinder structure), and (c) highest intensity (cone structure) in terms of CRI, CCT, DC, chromatic coordinates, intensity and structure height.

	CRI	CCT (K)	DC	(x,y)	Intensity	h (nm)
a	92.68	9609	0.0027	(0.2845, 0.2877)	100 %	0
b	93.84	9731	0.0027	(0.2837, 0.2869)	102.9 %	575
c	92.60	9593	0.0029	(0.2847, 0.2876)	125.8 %	450

calculated results are normalized to the one without any structure applied. It is obviously shown that cone structure could improve the light extraction efficiency as high as 25.8 %, which is much larger than the typical value of cylinder structure (2-3 %).

Among the simulation results, three examples have been selected and summarized in table 4.1. The CRI, CCT, distance to the Planckian locus (DC), (x, y) coordinate in the CIE 1931 chromaticity diagram, integrated intensity over the entire visible range, structure type, and structure height of these three examples have been compared. There is no structure applied for example a. Example b has the highest CRI of 93.84, and the extraction efficiency is 2.9 % higher than that of example a, which was achieved in a cylinder structure with height of 575 nm. The highest extraction efficiency improvement of 25.8 % was achieved in example c which was a cone structure with height of 450 nm. Its CRI value is almost the same as example a.

Transmittance curves and transmitted spectra of these three examples have been plotted in Fig. 4.6. Fig. 4.6a shows that the overall transmittance of the cone structure is much larger than that of cylinder structure, which is in good accordance with the results from Fig. 4.5d. Example b has a local maximum at around 440 nm in its transmittance curve and it enhances the transmittance of this area relatively larger than others (see Fig. 4.6b). We attribute this to one of the crucial reasons which lead example b to have the highest CRI.

Fig. 4.7a shows the locations of all the transmitted spectra in CIE 1931 (x, y) chromaticity diagram. Fig. 4.7b is the zoom-in area where the positions of example a, b, and c are highlighted. Blue and red dots stand for the cylinder and cone structures with varied structure height respectively. Blue dots have relatively wider distribution than red dots, so the distance of to the Planckian locus is varied in a larger level, which agrees with the results observed in Fig. 4.5c. In addition, cylinder

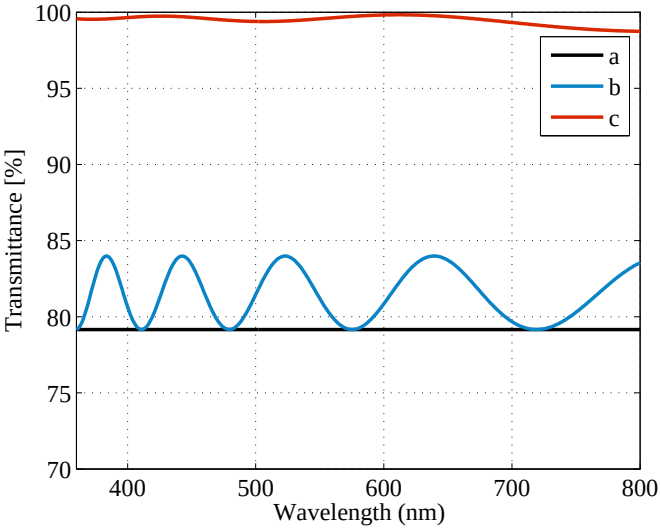

(a)

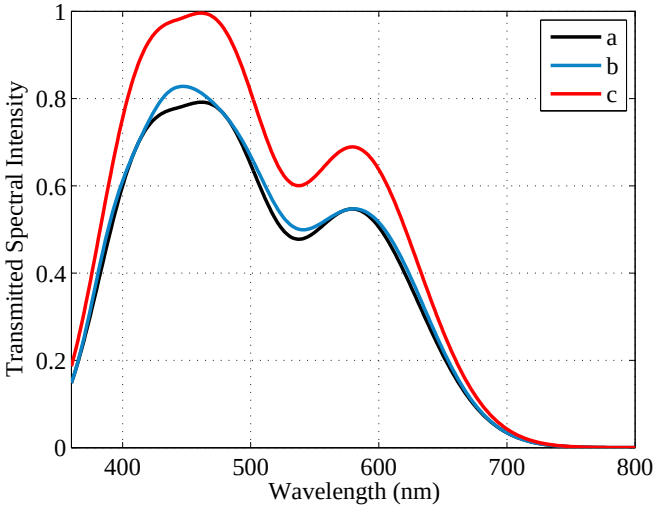

(b)

Figure 4.6: (a) Transmittance curves, and (b) transmitted spectra of the three examples a, b, and c listed in table. 4.1.

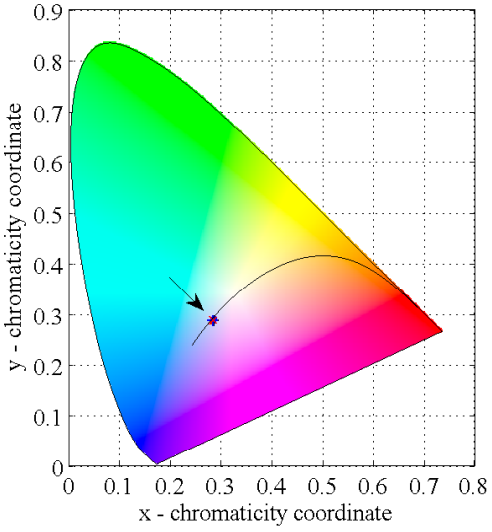

(a)

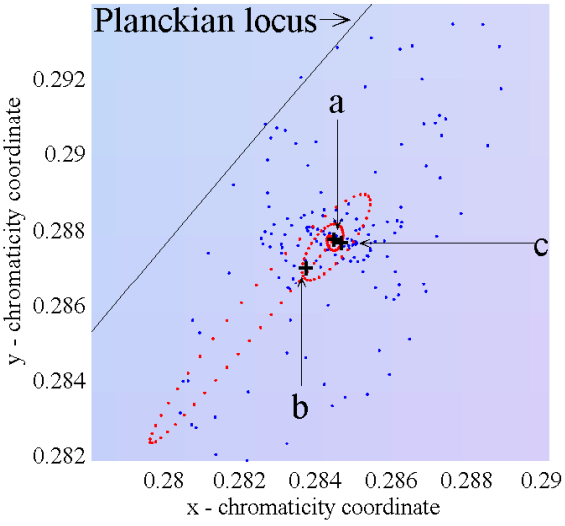

(b)

Figure 4.7: (a) Locations of all the transmitted spectra in CIE 1931 (x, y) chromaticity diagram, and (b) zoom-in for examples a, b, and c, where blue and red dots stand for the cylinder and cone structures with varied structure height, respectively.

structure shows the ability to obtain much lower CCT, and CCT value as low as 8930 K could be obtained. Nevertheless, the positions of the example a, b, and c are very close to each other, and all of the three examples have almost the same distance to the Planckian locus.

From our simulation, cone structure could lead to very large light extraction efficiency with improvement as high as 25.8 %, and the influence of structure dimensions on CRI and CCT is insignificant especially when the structure height is larger than 400 nm. Meanwhile, the highest CRI of around 94 could be achieved in a cylinder structure with structure height of 575 nm, the light extraction efficiency has only been enhanced by 3 % though. In addition, by applying cylinder structure with appropriate design, the CCT can be modified in a large range and the white light of 8930 K has been achieved.

In conclusion, We have theoretically investigated the influence of ARS on a monolithic white LED, and both cylinder and cone structures have been studied in the work. These simulation results provide very useful guidance for the future device fabrication. Cone structure could significantly enhance the extraction efficiency over the entire visible light range with an enhancement of up to 26 %. Due to the broadband transmission response, its CRI and CCT are very stable with varied structure dimension which is an advantage in the real fabrication. On the other hand, although the cylinder structure could only enhance the extraction efficiency by 3 %, the spectra response can be controlled by designing the structure as a thin film interferometer. Therefore, very high CRI could be achieved and CCT could be modified in a very large range under stringent processing control.

4.3 Impact of ARS on light extraction efficiency

It is noticed that, due to a smooth graded refractive index from the structure bottom to the top, nanocone structures can suppress the surface reflection of fluorescent SiC significantly from above simulation work. To further study the influence of cone structure profile on antireflection ability of fluorescent SiC, relevant calculation were carried out by using a commercial software RSoft based on the three dimensional RCWA algorithm. It is assumed that the linearly polarized incident light enters from air into the structure at normal incidence.

Cone structures arranged in the hexagonal grid were applied on flu-

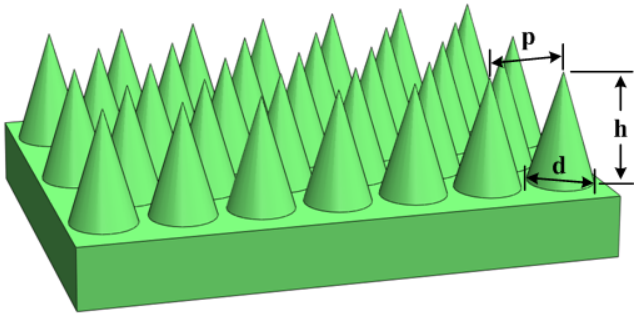

Figure 4.8: Schematic diagram of cone-shaped subwavelength structures arranged in the hexagonal grid; d, h, and p are bottom diameter, height, and period of the subwavelength structures respectively.

orescent 6H-SiC surface and the schematic diagram is shown in Fig. 4.8 where d, h, and p are bottom diameter, height, and period of the subwavelength structures respectively. In each calculation, cone structure height was varied from 200 to 1200 nm, structure bottom diameter was varied from 150 to 600 nm, and structure period was bottom diameter dependent. Structure period to bottom diameter ratio was varied from 1.3 to 1.8, and the reflectance calculation was performed in the spectral range of 350 to 800 nm. Contour plots of average reflectance are shown from Fig. 4.9a to 4.9f corresponds to different structure period to the bottom diameter ratio respectively.

Similar trend is obtained within all the calculation results, and generally a low average reflectance (below 5 %) could be achieved by having a high structure (above 600 nm) when the period is below 600 nm. On the other hand, short structure height and large period usually lead to a large surface reflectance value. The size of the region with lowest reflectance (the darkest blue region in the contour plots) depends on the structure period to bottom diameter ratio. It is seen that this region shrinks and moves toward the smaller period and larger height direction when the structure period to bottom diameter ratio increased from 1.3 to 1.8. This reveals that more dense structures could achieve low surface reflection within a relatively larger value range of structure height and period.

Although fabricating dense nanopatterns by using regular e-beam lithography needs more sophisticated technology control from the fabrication point of view, cone structures with height larger than 600 nm, period in the range of 300 to 450 nm, and structure period to bottom di-

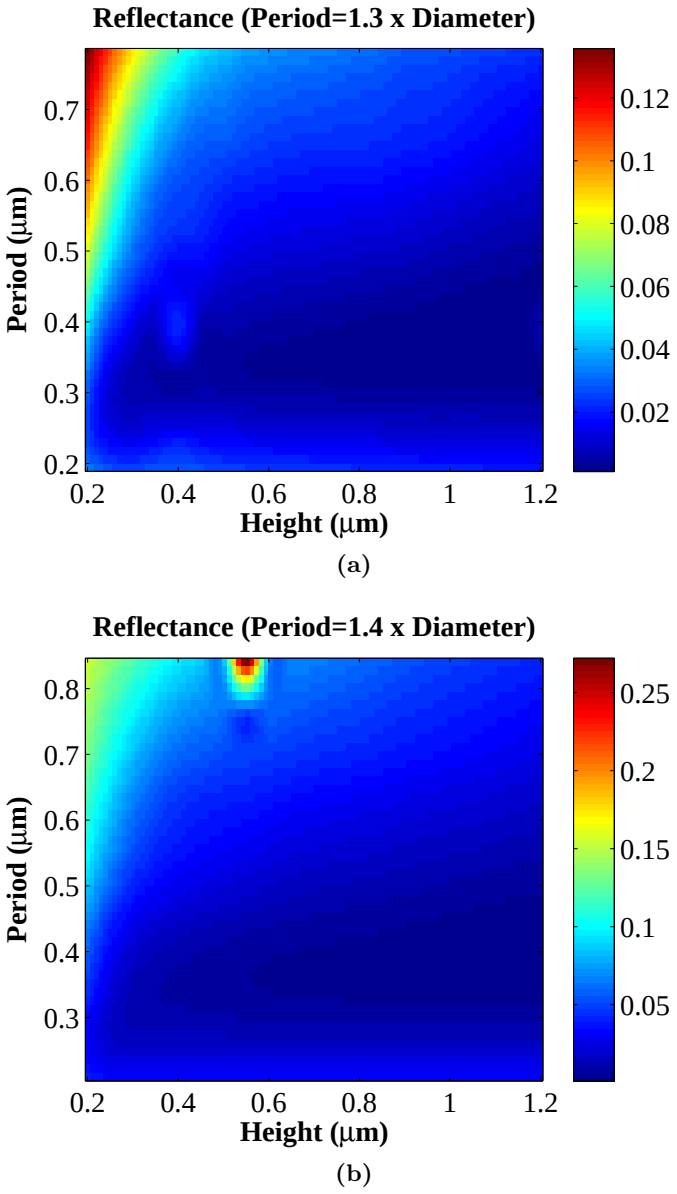

Figure 4.9: Calculated average reflectance in the spectral range of 350-800 nm with different structure height and period value when (a) period=1.3·diameter, and (b) period=1.4·diameter was applied.

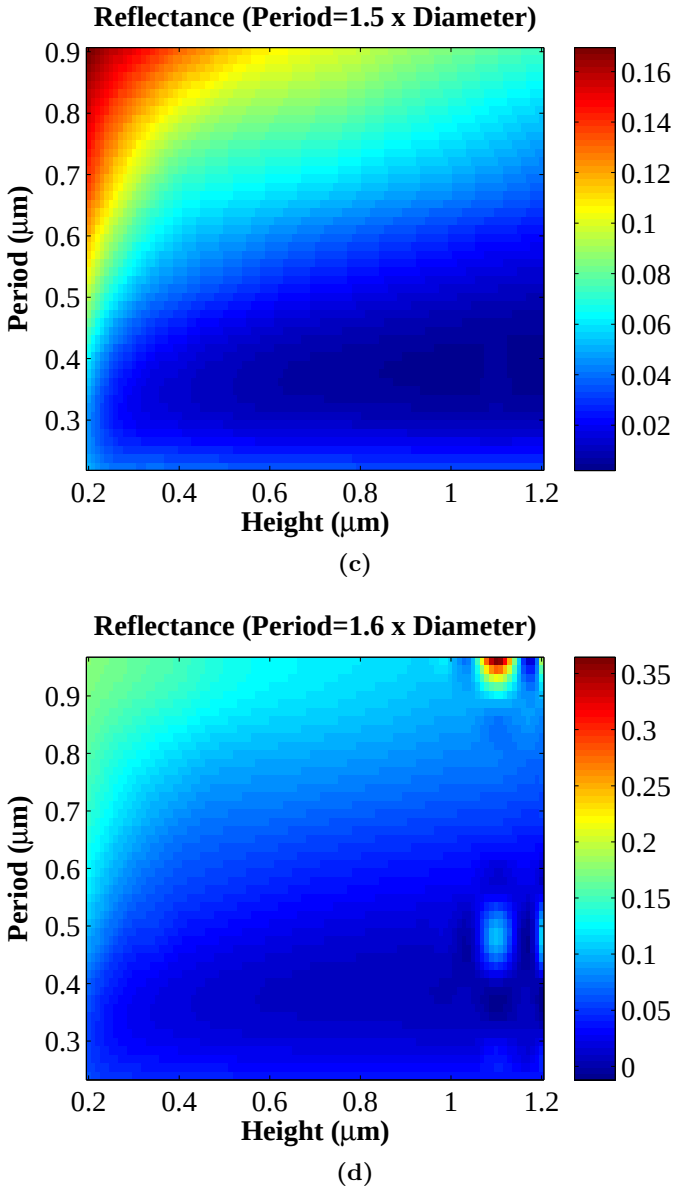

Figure 4.9: Calculated average reflectance in the spectral range of 350-800 nm with different structure height and period value when (c) period=1.5·diameter, and (d) period=1.6·diameter was applied.

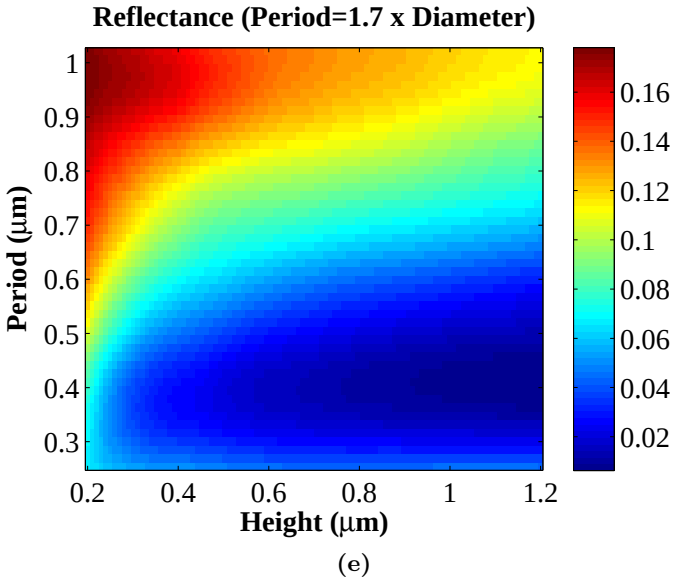

(e)

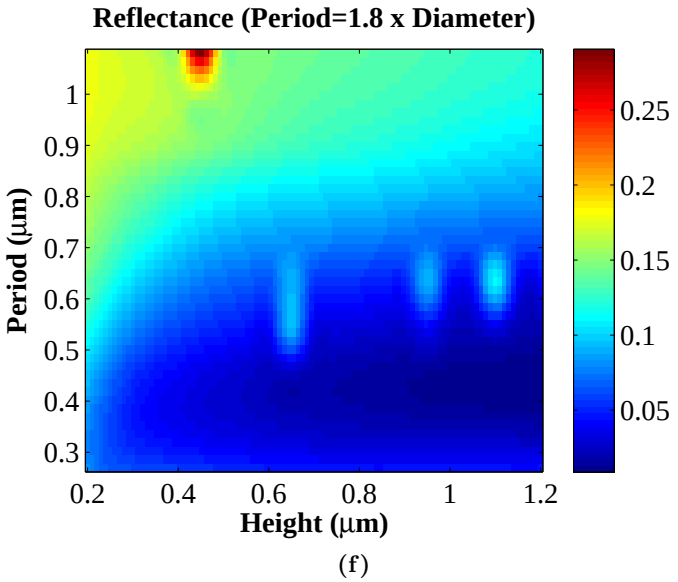

(f)

Figure 4.9: Calculated average reflectance in the spectral range of 350-800 nm with different structure height and period value when (e) period=1.7·diameter, and (f) period=1.8·diameter was applied.

ameter ratio less than 1.5 could be fabricated. As a result, an extremely low average reflectance below 2 % could be expected in the spectral range of 350-800 nm.

4.4 Summary

Influence of different ARS type on the fluorescent SiC based white LED was investigated in terms of CRI, CCT, and extraction efficiency. It is found that cone structure could enhance the extraction efficiency significantly over the entire visible light range with a structure height larger than 400 nm, and an enhancement of up to 26 % could be achieved. Meanwhile, its CRI and CCT are very stable with varied structure dimension because of the broadband transmission response. On the other hand, by applying cylinder structure, the spectra response can be controlled by designing the structure as a thin film interferometer. Therefore, higher CRI could be achieved and CCT could be modified in a very large range under stringent processing control, though the extraction efficiency was enhanced in a low level.

By applying the cone structures on fluorescent SiC, structure profile dependent surface reflection ability was examined. The results reveal that high structure and small period can lead to a low surface reflectance. Low structure period to bottom diameter ratio value corresponds to a possibilty of that low reflectance could be fabricated within a large structure profile range.

These calculation results provide very useful guidance for real ARS fabrication process. With carefully designed structure profile, low surface reflectance in a broad spectral range could be achieved. Both CRI and CCT could be improved or modified by adjusting the structure profile.

Chapter 5

Fabrication of antireflective subwavelength structures

In this chapter, several methods are demonstrated to fabricate periodic and pseudoperiodic Antireflective Structures (ARS) on Fluorescent Silicon Carbide (f-SiC) in order to enhance the light extraction. Fabrication processes are introduced in detail and the ARS have bee examined in terms of broadband surface reflectance and Angle-Resolved Photoluminescence (ARPL).

5.1 Periodic ARS by e-beam lithography

Firstly, we present an approach to fabricate a periodic cone-shaped ARS array on the Nitrogen-Boron (N-B) doped f-SiC by using Electron beam (E-beam) lithography for nanopatterning. Surface reflectance and ARPL measurements have been performed, and broadband antireflection and omnidirectional light harvesting enhancement are obtained after introducing the surface ARS.

5.1.1 Experimental details

The fabrication process is illustrated in Fig. 5.1. Firstly, the positive e-beam resist (ZEP520) was spin-coated on the SiC sample (Fig. 5.1a) and then pre-baked on a hot plate at 160°C for 2 minutes (Fig. 5.1b). By using the e-beam lithography (JEOL JBX9300FS) with a subsequent development process, the designed pattern was transferred to the e-beam resist coating (Fig. 5.1c). A hard mask material (chromium) layer

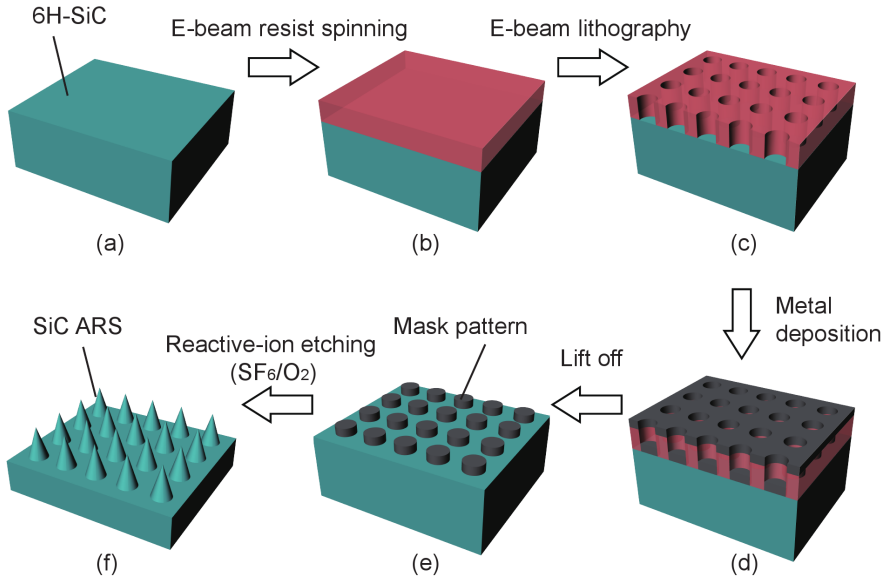

Figure 5.1: Schematic illustrations of periodic SiC ARS fabrication process steps (a)-(f).

was then deposited on the patterned SiC by using e-beam evaporation (Fig. 5.1d). Followed by a lift-off process, the dot-shaped pattern of chromium was obtained as a hard mask layer (Fig. 5.1e). The dry etching process using SF_6 and O_2 precursors was carried out in the RIE system (STS cluster system C010). During the etch process, the radio frequency power (100 W), process pressure (30 mT), and gas flow rates (20 sccm SF_6, 5 sccm O_2) of the RIE were carefully chosen. After 12 minutes etching, the cone-shaped ARS with designed configuration (bottom diameter of 240 nm, pitch of 340 nm, height of 1.2 μm, and hexagonal arrangement) were finally formed on the SiC surface (Fig. 5.1f).

Sample is then characterized by scanning electron microscope (SEM: Carl Zeiss SMT GmbH 1550). SEM figures of the SiC sample in different step of the ARS fabrication process have been shown in Fig. 5.2. Fig. 5.2a to Fig. 5.2c show the top-view of processed sample after e-beam lithography with developement, lift-off, and RIE process respectively, corresponds to the step in Fig. 5.1(d) to 5.1(f) respectively. Fig. 5.2d shows an oblique-view of the fabricated ARS on SiC surface. It is seen that designed ARS configuration could be obtained after this fabrication

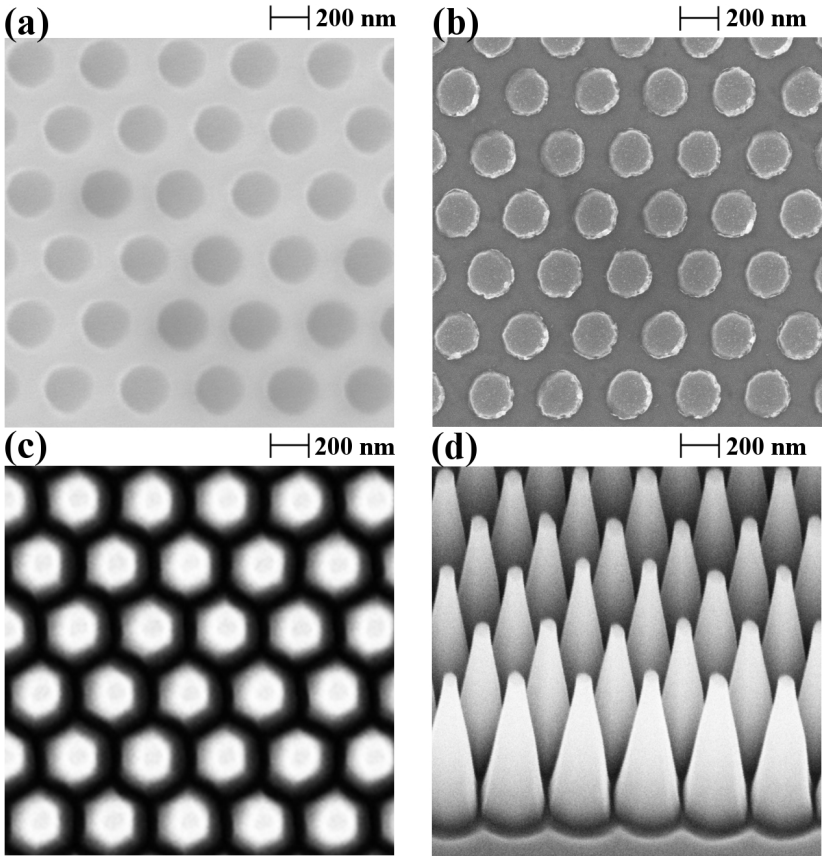

Figure 5.2: Top-view SEM figures of the processed sample after (a) e-beam lithography with developement, (b) lift-off, and (c) RIE process; (d) an oblique-view SEM figure of fabricated ARS on SiC sample surface.

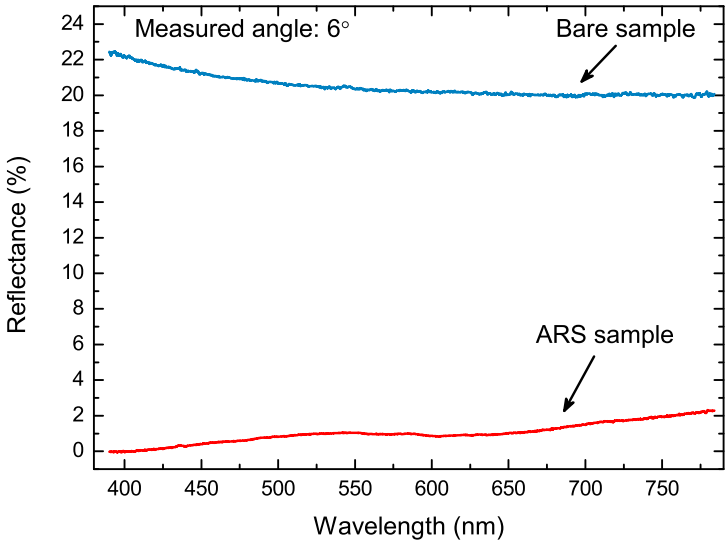

Figure 5.3: Reflectance spectra of the SiC samples with and without ARS (measured at 6°).

process.

The surface reflectance of the bare and ARS SiC samples were measured by a goniometer system (see Fig. 3.6) at a measured angle of 6°, where 0° is the direction normal to the sample surface. The reflectance spectra were measured from 390 to 785 nm which covers the entire visible spectral range (typically from 390 to 750 nm). Room temperature ARPL spectra of the bare and ARS SiC samples were also acquired by the same goniometer system. A 377 nm diode laser was used as the excitation source which was normal to the sample surface and the detected emission angle varied from 16 to 80°.

5.1.2 Results and discussion

The surface reflectance spectra are shown in Fig. 5.3. It is seen that the surface reflection is effectively suppressed by applying the SiC ARS. The average reflectance over the measured spectral range decreased from 20.5 % to 1.01 % and the minimum reflectance close to 0 was observed at around 400 nm from the ARS SiC sample. Although the reflectance starts to increase at above 680 nm, the reflectance over the entire visible spectral range is below 2 %. This result suggests that the SiC ARS is an effective way to suppress the surface reflection for the f-SiC sample

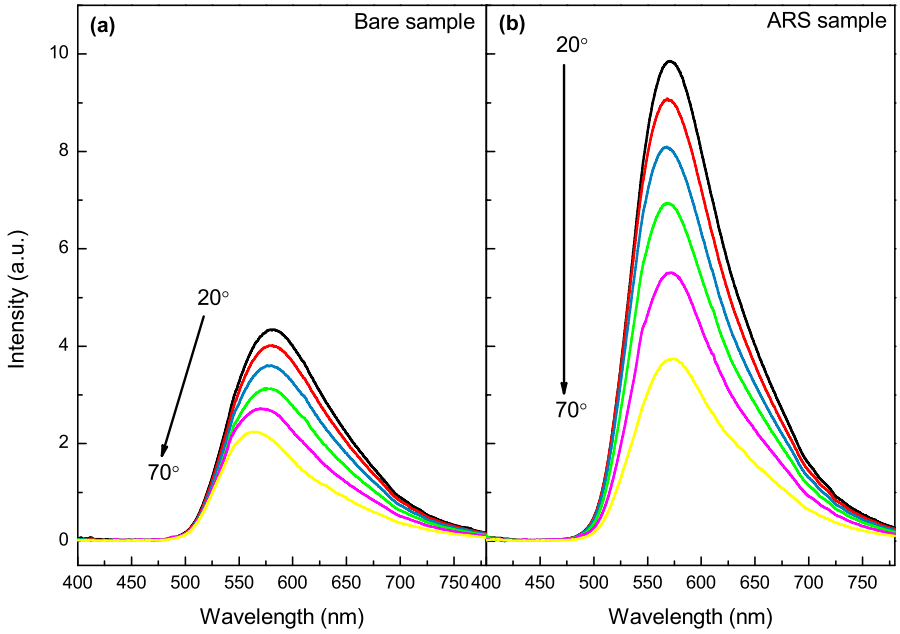

Figure 5.4: Angle-resolved photoluminescence spectra from 20 to 70° of (a) Bare, and (b) ARS SiC samples

in the whole visible spectral range.

The ARPL spectra are illustrated in Fig. 5.4. The broad DAP band luminescence of the N-B doped f-SiC has a peak wavelength at round 578 nm and a full width at half maximum of 110 nm which is a merit as wavelength-conversion material. From Fig. 5.4a, it is seen that the luminescence intensity of the bare SiC decreases together with a blue shift of the peak wavelength as the emission angle increases from 20 to 70°, which could be attributed to the Fabry-Pérot microcavity interference effect. In Fig. 5.4b, although the luminescence intensity of the ARS SiC also decreases with larger emission angle, the peak wavelength remains the same which is due to the elimination of the Fabry-Pérot microcavity interference effect by introducing the ARS on the SiC surface.

The ARPL enhancement of the ARS SiC is shown in Fig. 5.5. It is seen that the luminescence intensity is enhanced by larger than 91 % from the emission angle of 16 to 70°, and the highest enhancement of 115.4 % is obtained at the emission angle of 16°. Although the enhancement starts to decrease dramatically from 70°, the luminescence intensity of the SiC is significantly enhanced in a very large emission

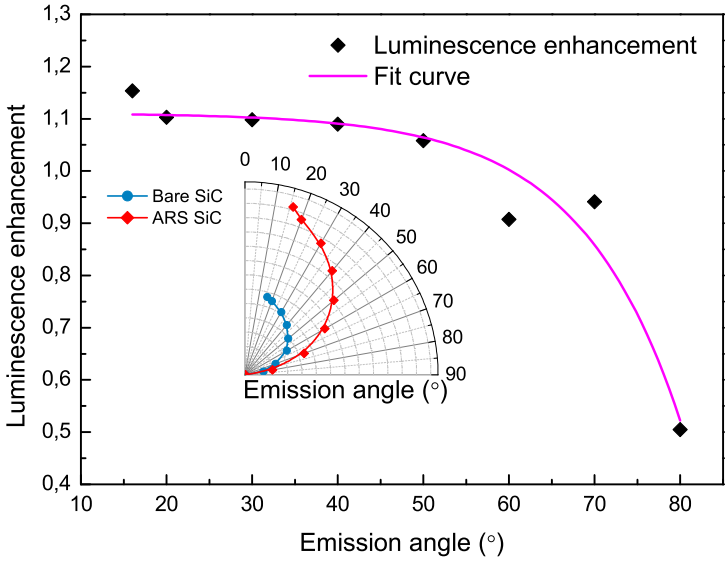

Figure 5.5: Angle-resolved luminescence enhancement of SiC sample after introducing periodic ARS; inset: spatial emission pattern of the two samples.

angle range.

5.1.3 Conclusion

In this work, periodic ARS have been fabricated on f-SiC to enhance the broadband light extraction efficiency by using the e-beam lithography for nanopatterning and RIE for dry etching. Broadband antireflection characteristics show that 6H-SiC with ARS suppress the average surface reflection significantly from 20.5 % to 1.01 % over a wide spectral range of 390-784 nm. The luminescence intensity of the f-SiC could be enhanced in the whole emission angle range of 16 to 70°. It maintains an enhancement larger than 91 % up to the incident angle of 70°, while the largest enhancement of 115.4 % could be obtained at 16°. Applying periodic ARS on f-SiC could also preserve the luminescence spectral profile at a large emission angle by eliminating the Fabry-Pérot microcavity interference effect.

5.2 Periodic ARS by nanosphere lithography

To fabricate a periodic ARS array (of nanopillars, nanocones, or nanodomes) on the SiC, it is indispensable to have an etching template with subwavelength dimension. Compared with commonly used e-beam lithography and nanoimprint lithography processes, nanosphere lithography is a time-saving and cost-efficient nanopatterning technique for subsequent etching process and it is also a promising way for large-scale production [121–127]. Besides, self-assembly nanospheres with different material choices and dimensions are commercially available, thus providing a platform in various applications.

In this section, we propose a novel method to fabricate a nanodome array, demonstrated on N-B co-doped f-SiC, by using RIE process with self-assembled polystyrene (PS) nanospheres as a template. A single-step etching process was applied to fabricate such a nanodome array on a 190 μm thick f-SiC sample. Average surface reflection over the whole visible spectral range is significantly suppressed and an omnidirectional luminescence enhancement is also achieved. The antireflection and luminescence enhancement performance of the nanodome array are also compared with the ones of a nanocone array fabricated by the same method but using a silica nanospheres array as an etching template.

5.2.1 Experimental details

Schematic drawing of the detailed fabrication processes of the nanodome array is illustrated in Fig. 5.6a to 5.6c. Firstly, a monolayer hexagonal-close-packed array of PS nanospheres with a diameter of 600 nm (size dispersion of 1 %) is formed on a pre-treated SiC sample surface by a self-assembly method (see Fig. 5.6a). Subsequently, the SiC sample is subjected to RIE for pattern transfer, where the PS nanospheres monolayer serves as an etching template (see Fig. 5.6b). Due to the isotropic nature of the chemical etching from the plasma gases and directional bombardment of accelerated ions from physical etching in RIE, the PS nanospheres are etched away in an anisotropic fashion, i.e. with different etching rates for the vertical and lateral directions. Consequently, the nanospheres become thinner and their transverse diameters also decrease gradually. The exposed area of the underlying SiC substrate then increases. Despite the etching rate of SiC, the structure profile of the fabricated SiC ARS also depends on the vertical (ER_V) and lateral etching rate (ER_L) of the template material. If the average ER_V of

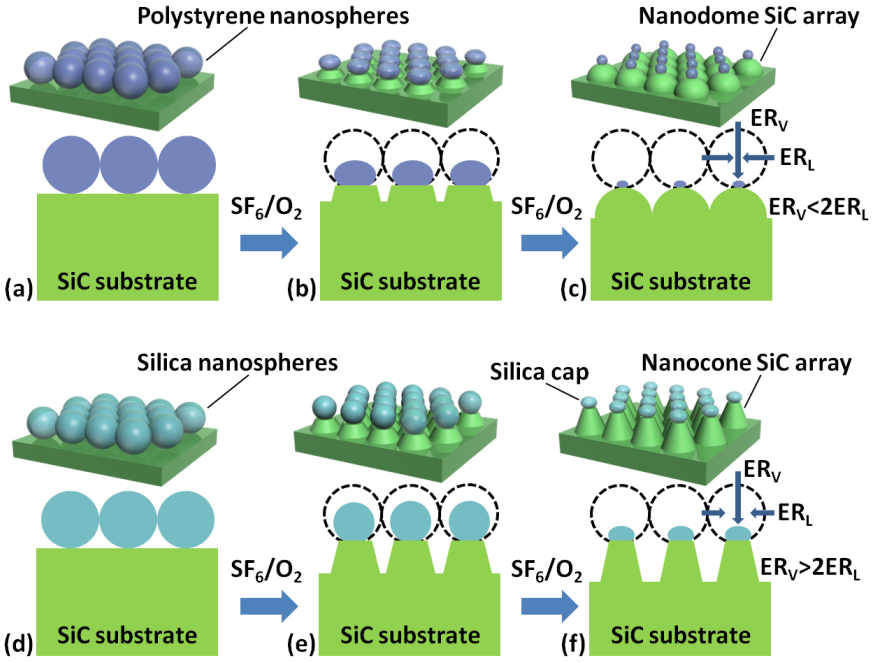

Figure 5.6: Schematic diagram showing the detailed fabrication process of nanodome and nanocone array on f-SiC samples. (a)/(d) Formation of self-assembled polystyrene/silica monolayer nanospheres as etching template, (b)/(e) etching process by RIE with SF6 and O2 gases, (c)/(f) formation of the nanodome/nanocone array on f-SiC samples, thanks to the different vertical and lateral etching rate of polystyrene/silica nanospheres.

the nanospheres is lower than twice of its average ER_L, the nanospheres will be etched out firstly in the lateral direction. Due to this, ARS in a nanocone-shape with a sharp-tip or a nanodome-shape is achieved eventually. These types of structures have attractive aspect ratios with a smooth graded refractive index from the bottom of the structure to the top, providing a promising way for broadband antireflection purposes. In our experiments, the average ER_V and ER_L of the PS nanospheres are around 87 and 61 nm/minute respectively under the optimized RIE conditions. Finally, the f-SiC nanodome array can be achieved by using PS nanospheres as the unique template (see Fig. 5.6c).

In order to compare with the nanodome array sample, a nanocone array was also fabricated using another nanospheres template and the fabrication process is illustrated from Fig. 5.6d to 5.6f. A monolayer hexagonal-close-packed array of silica nanosphere with a diameter of 500 nm (size dispersion of 1 %) is used here as the etching template (see Fig. 5.6d). For comparison, the same RIE conditions were then applied (see Fig. 5.6e). In this case, the average ER_V (77.8 nm/minute) of the silica nanospheres is much larger than twice of the average ER_L (16.7 nm/minute). Thus the silica nanospheres are etched out firstly in the vertical direction and a frustum nanocone array is then obtained. It is known that the frustum nanocone has a large refractive index difference between the frustum surface and air, thus limiting its antireflective functionality. Here, a residual silica cap layer with an intermediate refractive index (1.54) between the refractive index of air (1) and 6H-SiC (2.68) sitting on the top of the frustum nanocone (see Fig. 5.6f) is used to relieve the large refractive index difference.

The etching process was carried out by using a RIE etcher (STS cluster system C010) in a flow of SF6 and O2. By applying machine conditions optimized for SiC etching, nanodome and nanocone arrays were fabricated by mixing of SF6 and O2 gases (24 and 6 sccm) at a R.F. power of 100 W and chamber pressure of 30 mT.

Fig. 5.7a to 5.7c are the oblique view SEM images of the monolayer close-packed nanospheres (the silica spheres sample is taken as an example here), frustum nanocone array with silica caps (hereinafter referred to as nanocone array), and nanodome array, respectively. The inset of Fig. 5.7a shows a top-view SEM image of the self-assembled nanospheres arranged in a hexagonal form. The frustum nanocone with a structure height of about 420 nm was fabricated after 4 minutes and 30 seconds etching process together with a residual silica cap layer with

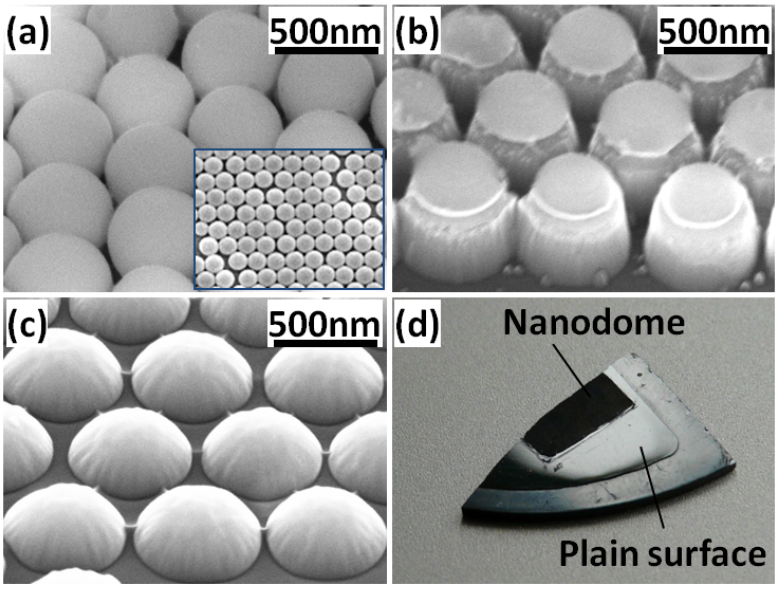

Figure 5.7: Oblique view SEM images of the (a) monolayer close-packed silica nanosphere, (b) fabricated frustum nanocone array with a silica cap, and (c) fabricated nanodome array respectively. The inset of (a) shows the top-view SEM image of the nanosphere pattern. (d) A photograph of SiC sample with plain surface (lower right part) and partially covered by a nanodome array (upper left part).

a height of 150-210 nm due to etching imperfection. On the other hand, after 5 minutes etching, a nanodome array was reached with a structure height of around 450 nm by using the PS nanospheres as the template. Despite the near-perfect spherical shape and smooth surface, nanodome structures also have a low aspect ratio which is desired for further electrode material (metal/ITO) deposition. A vertical etch rate of around 90 nm/minute for SiC is achieved in both experiments. Fig. 5.7d shows a photograph of the SiC sample with plain surface (lower right part) and partially covered by nanodome array (upper left part). The surface color of the sample turns from bright grey to black after surface patterning, indicating a significant suppression of surface reflection.

Surface reflectance in a broadband spectral range from 390 nm to 785 nm were measured by using a goniometer system (see Fig. 3.6). A halogen lamp as a broadband light source was connected to the transmitter arm of the goniometer and the receiver arm was connected to an optical spectrometer (Instrument System, CAS140B). SiC samples were mounted on the sample stage and the reflection spectra were measured with an incidence angle of 8° with respect to the surface-normal direction. The same goniometer used in the reflectance measurements was also applied in ARPL measurements. A 377 nm diode laser was connected to the tranmitter arm as the excitation light source and the SiC sample was optically excited from its back side at room temperatue conditions. The detection angle of the receiver arm varied from 0° (surface-normal direction) to 80° with a step of 10° and the corresponding photoluminescence spectra were then acquired

5.2.2 Results and discussion

In order to demonstrate the broadband antireflection effect, the measured reflectance spectra of different samples are compared in Fig. 5.8a. In the measured spectral range, the average reflectance of the plain sample is around 21.0 %. An antireflection enhancement is obtained after surface patterning. The reflectance of the nanocone sample was maintained below 8.0 % between 400 and 500 nm. It then increases with the wavelength up to 630 nm, while the average reflectance is about 13.1 %. Especially, the average reflectance of the nanodome sample is dramatically suppressed to 3.3 % and the reflectance is below 6.0 % through the whole range. Numerical calculated reflectance were implemented by a rigorous coupled-wave analysis (RCWA) model and compared with the experimental results in Fig. 5.8a. The measured reflectance of the

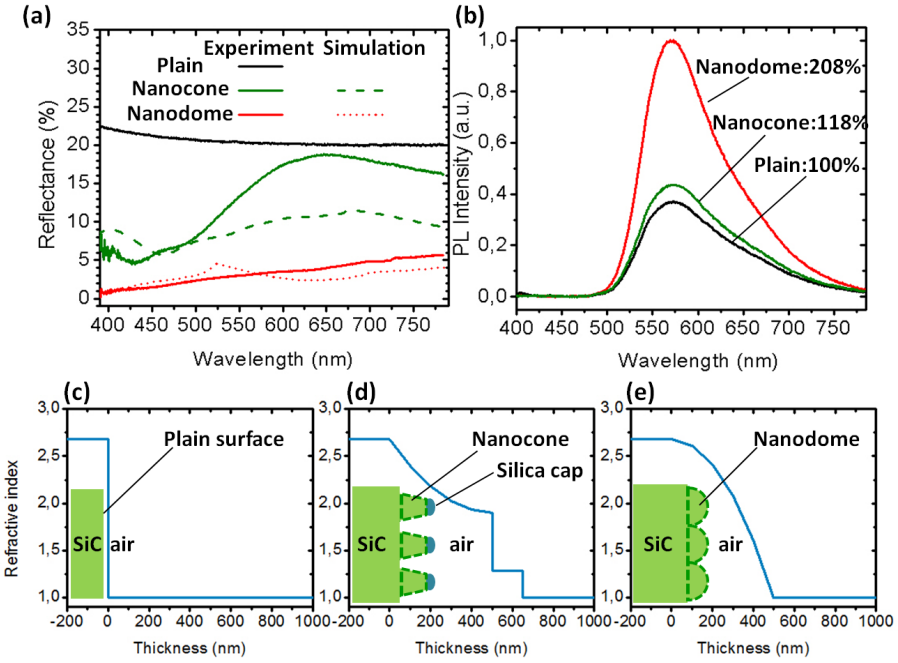

Figure 5.8: (a) Experimental and RCWA-simulated optical reflectance and (b) photoluminescence spectra of the f-SiC sample with a plain surface, a nanocone array, and a nanodome array, respectively. Effective refractive index profiles of the interfaces between air and SiC with (c) a plain surface, (d) a nanocone array, and (e) a nanodome array.

nanocone sample shows a higher value than its calculated one, probably due to the size variation of the silica layer caused by etching imperfection. By contrast, nanodome sample exhibits a fairly good match between the measured and calculated reflectance.

Photoluminescence measurements were then conducted by using a diode laser with a peak wavelength of 377 nm as an excitation light source. The f-SiC sample exhibits a broad luminescence peaked at 575 nm and the luminescence is enhanced after surface nanostructuring. As seen in Fig. 5.8b, the nanocone sample supports an 18 % luminescence enhancement at the emission angle normal to the sample surface. In contrast, the luminescence of the nanodome sample was enhanced significantly by 108 %.

The photoluminescence results are in a good consistency with the results from the surface reflectance measurements. The experimental observations are explained by the effective refractive index (n_E) profiles of the interfaces between air and SiC samples with the plain surface, the nanocone array, and the nanodome array, as shown in Fig. 5.8c to 5.8e. The n_E profile follows n_E=fn_1+(1-f)n_2, where n_1 and n_2 are the refractive indices of f-SiC (n=2.68) and air (n=1) respectively, and f is the filling factor weighted by the structure volume at different structure heights. The refractive index changes abruptly from 2.68 to 1 across the plain interface (Fig. 5.8c), which causes a large internal reflection. The frustum nanocone structure has a n_E that changes gradually from the structure bottom to the frustum surface (around n=1.82 by calculation). Then the large refractive index difference between the frustum surface and air can be relieved by the silica cap layer with an intermediate refractive index of around 1.54 (Fig. 5.8d). For the nanodome sample, the diameter of the dome structure shrinks gradually from the bottom to the top, thus resulting in a graded transition of the n_E (Fig. 5.8e). As a result, nanodome structures are anticipated to allow for considerable reflection suppression over a broadband spectral range as well as a luminescence enhancement. These expectations are supported by our experimental results as shown in Fig. 5.8a and 5.8b.

Angular emission profiles from ARPL measurements are illustrated in Fig. 5.9a for both nanodome and plain samples. A broadband extraction enhancement is obtained for the nanodome sample at all the tested angles. Especially, a large enhancement over 100 % is obtained at small emission angles. Therefore, the nanodome structure acts as a micro-lens to confine the light transmission in the vertical direction. Numerical sim-

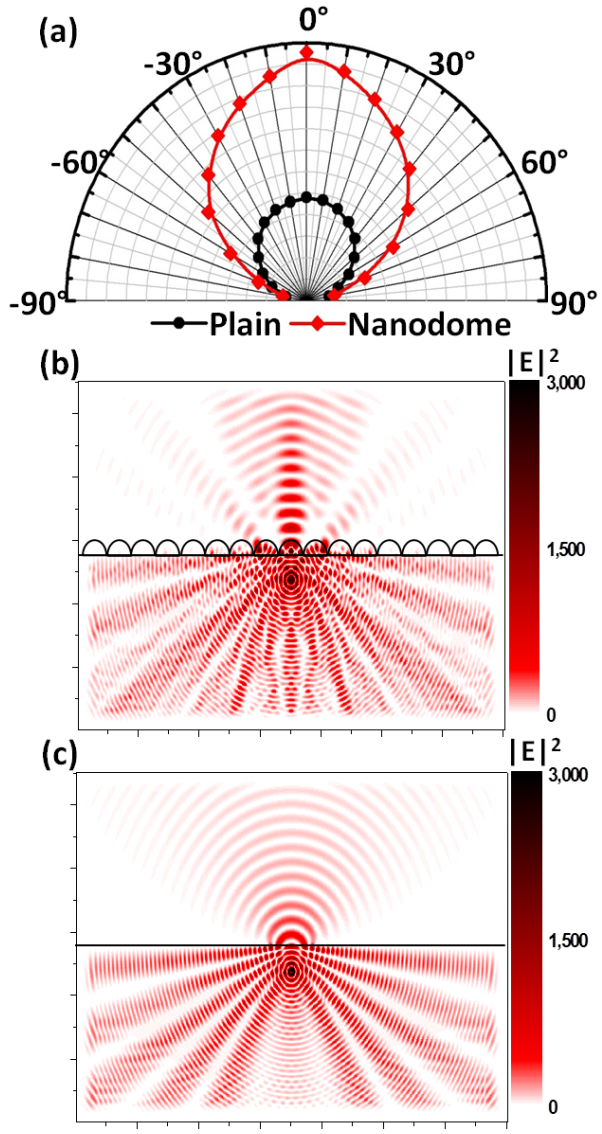

Figure 5.9: (a) Angular emission profiles for SiC samples with a plain surface and a nanodome array. Electric field distribution based on FDTD simulations of wave propagation for (b) plain SiC and (c) nanodome SiC, respectively.

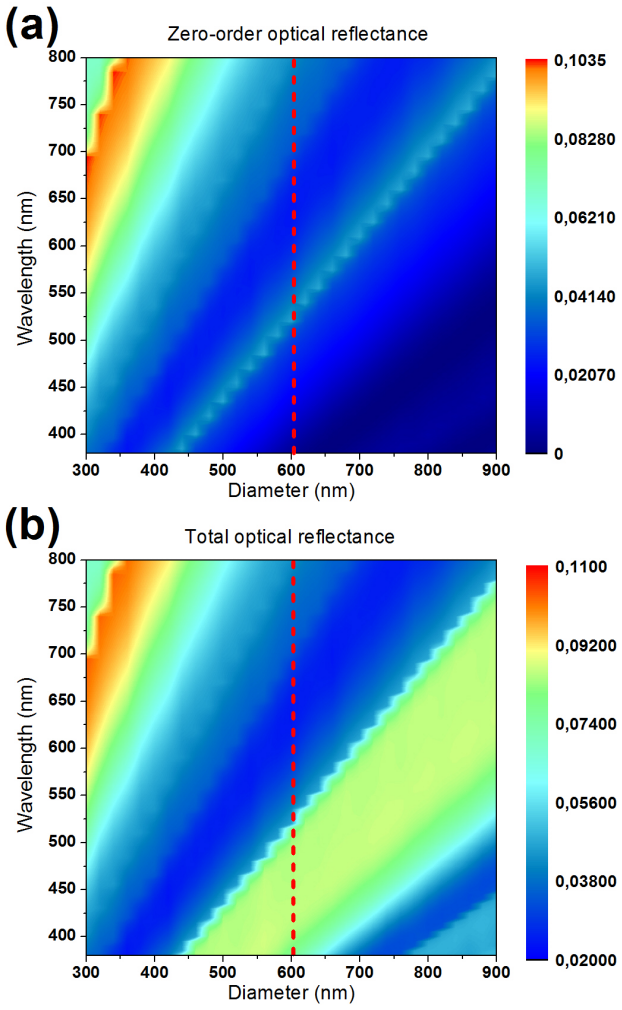

Figure 5.10: Calculated (a) zero-order and (b) total optical reflectance of nanodome array with different sphere diameter.

ulations based on a Finite-Difference Time-Domain (FDTD) method are also performed to complement the experimental results. Fig. 5.9b and 5.9c show the simulated results of wave propagation for the nanodome and plain samples. The emitter is mimicked by a point source excitation. It is seen that a stronger light extraction was observed from the nanodome sample and the transmitted light was more focused, which are consistent with the experimental observations.

In order to estimate the influence of the sphere diameter on the optical antireflection enhancement, we illustrated in Fig. 5.10 the zero-order and total optical reflectance of a nanodome array as a function of the sphere diameter calculated by a RCWA model. The sphere diameter varies between 300 and 900 nm. We again observed a fairly low reflectance for the nanodome with a diameter of 600 nm as we used (dash line in the figure), especially in the region of 550-650 nm where the luminescence peak located. Moreover, by tuning the sphere size, the antireflection response to the wavelength can be adjusted. Therefore, this optical property can be designed for different wavelength purpose.

5.2.3 Conclusion

In conclusion, we have demonstrated a novel approach to fabricate nanodome arrays on f-SiC. This attractive approach relies on single-step RIE with self-assembled monolayer PS nanospheres as a template. Compared with either a plain sample or a nanocone array, the nanodome array allows a graded transition of the effective refractive index from the structure bottom to the surface which leads to a significant reflectance reduction from 21.0 % to 3.3 % in the spectral range of 390-785 nm. A luminescence enhancement in a large emission angle range is achieved and the nanodome array significantly improves the light directional properties. The results are further supported by FDTD simulations. Related applications such as solar cells and optical detectors could also benefit from the excellent antireflection performance by using this low-cost and scalable method.

5.3 Pseudoperiodic ARS by self-assembled nanopatterning

In this section, we fabricated a pseudoperiodic ARS array on SiC by using nanopatterned Au mask made from Rapid Thermal Processing

(RTP) method. Compared with normal e-beam lithography, RTP of thin metal films is one of the fast processes for the fabrication of the pseudoperiodic self-assembled nanopatterns which could be used as the etching mask for dry etching [128–130]. To achieve significant antireflection improvement, we investigated systematically the effect of the RIE conditions as well as the deposited Au film thickness on the antireflection properties of the fabricated pseudoperiodic SiC ARS. Furthermore, applying pseudoperiodic ARS on the f-SiC to achieve the omnidirectional luminescence enhancement over the entire visible spectral range has been demonstrated.

5.3.1 Experimental details

The fabrication process of pseudoperiodic ARS is schematically illustrated in Fig. 5.11. Firstly, a 10 nm Au layer was deposited on the SiC surface by using e-beam evaporation method (Fig. 5.11a). Then the sample was annealed at 350°C for 10 minutes in N_2 ambient by using the RTP method (Jipelec RTP), and the thin Au layer on the SiC surface were agglomerated into nano-islands which contain the minimum surface energy (Fig. 5.11b). Thereafter, RIE with SF_6 and O_2 gases mixture (4:1) for 10 minutes was applied and the pseudoperiodic cone-shaped ARS were formed on the SiC surface by using the Au nano-islands as a mask layer (Figs. 5.11c-5.11e). Finally, the residual Au were removed by using iodine based solution (Fig. 5.11f).

The antireflection performance of ARS usually depends on the structure profile. For example, from the previous work, it is found that structure height is a crucial factor affecting the antireflection ability for cone-shaped ARS and high structures are usually required to achieve fairly good antireflection performance on SiC. To obtain the suitable ARS profile with significantly suppressed surface reflectance, the RIE conditions (gases flow rates, RF power, and chamber pressure) and the deposited Au film thickness have been optimized in a large range. The optimization process have been done on the polished epi-ready surface of commercial n-type 6H-SiC substrates with background nitrogen doping level (SiCrystal AG). RIE conditions were optimized in two steps to achieve more time-saving and precise controlled process. The first rough optimization step was done in a large value range with a large step and the second fine one was done in a small range with a small step based on the optimal results obtained from the first optimization. The optimization range and step of RIE conditions and deposited Au film

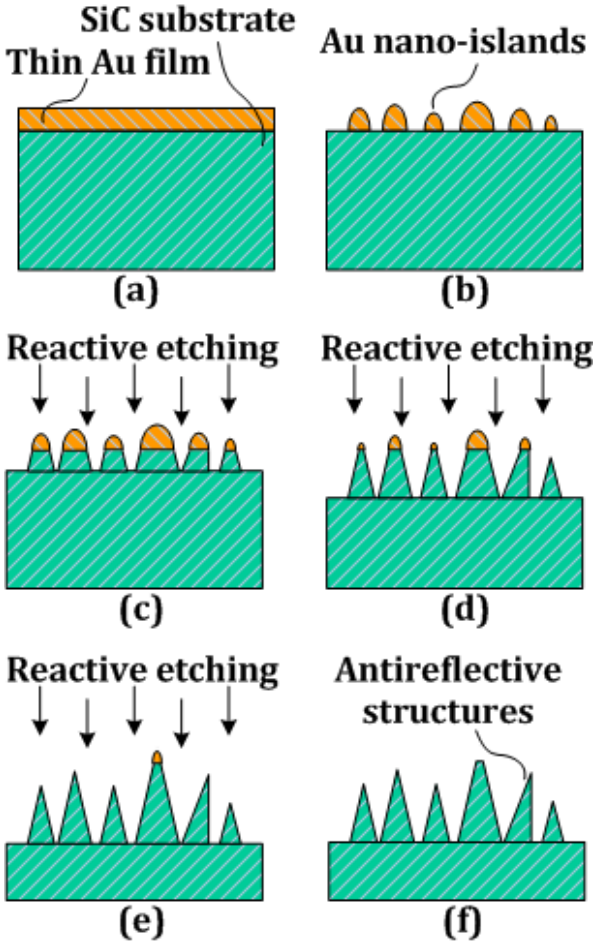

Figure 5.11: Schematic illustrations of the pseudoperiodic SiC ARS fabrication process steps: (a) Au film deposition, (b) rapid thermal processing, (c)-(e) reactive-ion etching, and (f) remove of residual Au.

Table 5.1: Optimization range and step of RIE conditions and deposited Au film thickness (fixed SF_6/O_2 flow rate ratio of 4/1 was applied during the whole process).

	First optimization	Second optimization
SF_6 flow rate (sccm)	12-28 (step: 4)	16-24 (step: 1)
RF power (W)	50-150 (step: 20)	85-120 (step: 5)
Chamber pressure (mT)	10-35 (step: 5)	22-36 (step: 2)
Au film thickness (nm)	5-12.5 (step: 2.5)	

thickness were listed in table 5.1.

To demonstrate the broadband antireflection performance of each sample, its surface reflectance at normal light incidence was then characterized. The reflectance has been measured by using a fluoresence microscope with proper light source and detector. The measured spectral range is from 390 to 784 nm. Furthermore, ARPL measurement of f-SiC sample has been performed by using a goniometer system, and a 377 nm diode laser as the excitation source. The excitation laser beam was normal to the sample surface, and the detection angle ranged from 20° to 80° in a step of 10°.

5.3.2 Results and discussion

RIE conditions optimization

Fig. 5.12a shows the average reflectance of the pseudoperiodic ARS fabricated with SF_6 flow rate in the range of 12-28 sccm with variable steps. During the whole process, 20 % addition of O_2 is always applied to get a higher etch rate. The RF power, chamber pressure, and etch time were fixed to 100 W, 30 mT, and 10 minutes respectively. Firstly, a large step of 4 sccm was applied for the SF_6 flow rate scan from 12 to 28 sccm. Then a fine scan with a step of 1 sccm was applied around the reflectance minimum. The average reflectance decreases from 3.15 % to 2.47 % when the SF_6 flow rate increases from 12 to 18 sccm. However, it increases to 2.60 % when the SF_6 flow rate increases further to 28 sccm. The inset two SEM figures show the fabricated ARS with SF_6 flow rate of 12 and 18 sccm corresponding to the highest and lowest reflectance respectively. Under the condition of 18 sccm SF_6, an etch rate of around 78 nm/minute was obtained, and the average aspect ratio (structure height to bottom diameter ratio) is about 2.5-4. It is seen that SF_6 flow rate has a relatively weak influence on the ARS profile, and

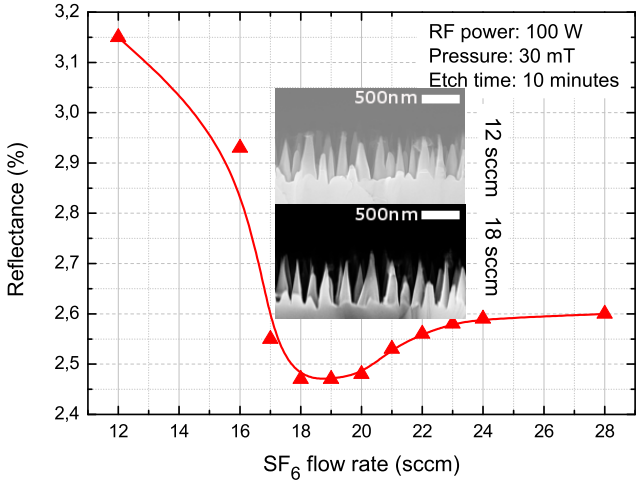

(a)

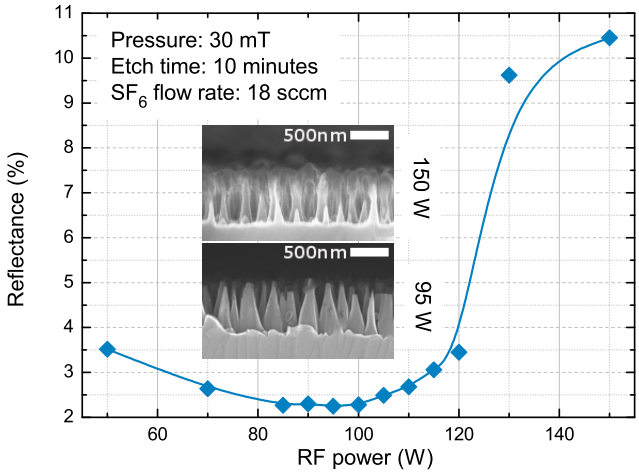

(b)

Figure 5.12: Reflectance measurements on the SiC substrates for the optimization of (a) SF_6 flow rate, (b) RF power; inset two SEM figures in (a), (b) show the cross-sectional view of fabricated pseudoperiodic SiC ARS with the corresponding parameter which have the highest (upper figure) and lowest (lower figure) measured reflectance after the optimization process of SF_6 flow rate, RF power respectively.

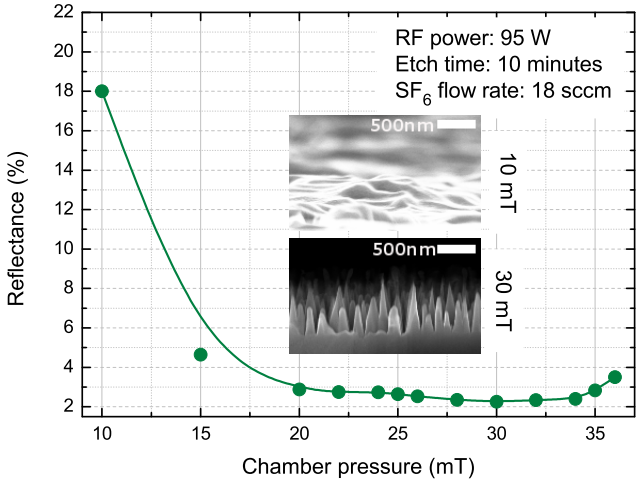

(c)

Figure 5.12: Reflectance measurements on the SiC substrates for the optimization of (c) chamber pressure; inset two SEM figures in (c) show the cross-sectional view of fabricated pseudoperiodic SiC ARS with the corresponding parameter which have the highest (upper figure) and lowest (lower figure) measured reflectance after the optimization process of chamber pressure respectively.

reflectance lower than 3.15 % is obtained through the entire SF_6 flow rate scan range.

Then the RF power was scanned in the range of 50-150 W with variable steps and the average reflectance of corresponding fabricated ARS are shown in Fig. 5.12b. The chamber pressure, etch time, and SF_6/O_2 flow rates were fixed to 30 mT, 10 minutes, and 18/4.5 sccm respectively. A large step of 20 W was applied first when the RF power was scanned from 50 to 150 W. Then a fine scan with a step of 5 W was applied around the corresponding reflectance minimum. The average reflectance decreases from 3.50 % to 2.25 % when the RF power increases from 50 to 95 W. However, it increases significantly to 10.49 % when the RF power increases further to 150 W. The inset two SEM figures show the fabricated ARS with RF power of 150 and 95 W which corresponding to the highest and lowest reflectance respectively. It is found that the ARS fabricated with 150 W and 95 W have similar etch rate of around 81 nm/minute. However, ARS etched with 150 W have larger aspect ratio (6.1-9.8) than the one etched with 95 W (3.1-3.8). This indicates large RF power usually leads to high sputter etch rate of Au, and ARS with small aspect ratio have relatively lower surface reflectance from this

result.

Fig. 5.12c shows the average reflectance of ARS fabricated with chamber pressure in the range of 10-36 mT with variable steps. The RF power, etch time, and SF_6/O_2 flow rates were fixed to 95 W, 10 minutes, and 18/4.5 sccm respectively. A large step of 5 mT was first applied for the chamber pressure scan from 10 to 35 mT. Then a fine scan with a step of 2 mT was applied around the corresponding reflectance minimum. The average reflectance decreases dramatically from 18 % to 2.1 % when the chamber pressure increases from 10 to 30 mT. However, it increases to 3.8 % when the chamber pressure increases further to 36 mT. The inset two SEM figures show the fabricated ARS with chamber pressure of 10 and 30 mT corresponding to the highest and lowest reflectance respectively. It is found that ARS profile strongly depends on the chamber pressure. No cone-shaped ARS have been fabricated with a chamber pressure of 10 mT, because the Au nano-islands were sputterred out quickly under such low chamber pressure. At 30 mT, an etch rate of around 84 nm/minute was achieved, and the average aspect ratio was about 2.2-3.5.

From above results, it is observed that the nano-cone profile of SiC depends on the gases flow rates, RF power, and chamber pressure. The RIE conditions need to be optimized to achieve desired ARS profile. The optimal etch conditions obtained from the above optimization process are: RF power of 95 W, SF_6/O_2 flow rate of 18/4.5 sccm, and chamber pressure of 30 mT, which corresponding to an etch rate of 84 nm/minute and average aspect ratio of 2.2-3.5.

Metal film thickness optimization

In addition, different thickness of deposited Au film is also examinated for its influence on the fabrication of ARS. Figs. 5.13a-5.13d show the top-view SEM figures of the Au film with different deposited thickness (5, 7.5, 10, and 12.5 nm) after processed by RTP at 350°C for 10 minutes. It is seen that isolated nano-islands are obtained from 5 nm thick Au film after annealing. Connections between nano-islands start to appear when the Au film thickness increases and no isolated nano-islands could be observed when the Au film thickness is 12.5 nm.

By applying the optimized RIE conditions, pseudoperiodic ARS are fabricated on all the samples and the cross-sectional SEM figures are shown in Fig. 5.13e-5.13h correspondingly. Different Au film thickness leads to different size and thickness of the nano-islands after annealing

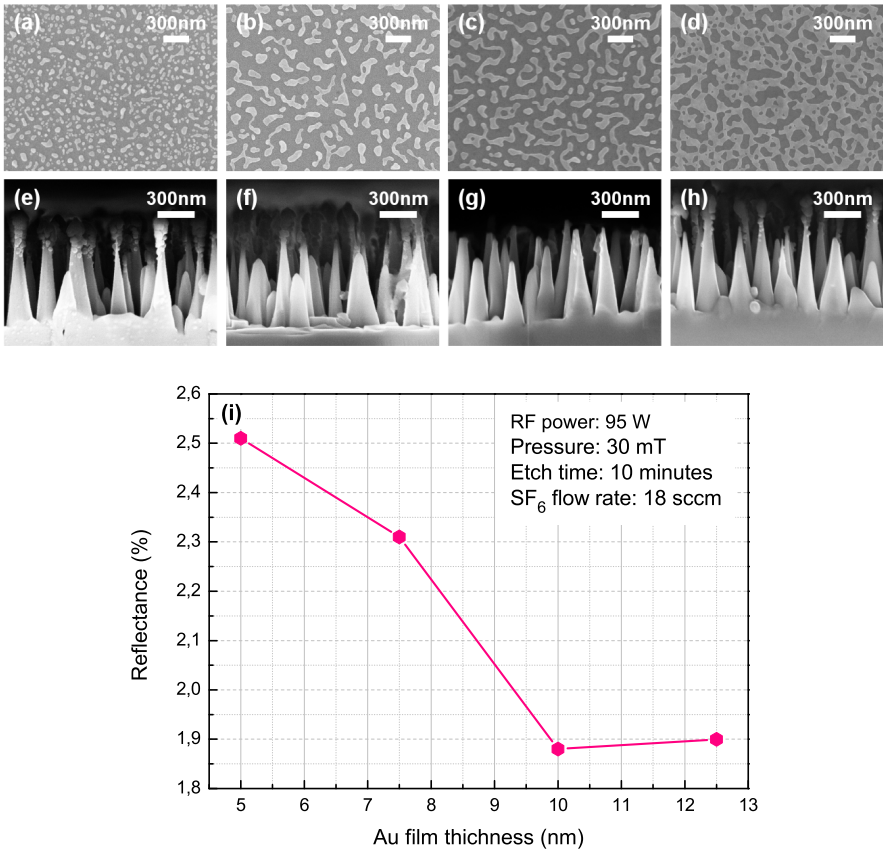

Figure 5.13: Top-view SEM figures of the SiC substrates annealed at 350°C with different deposited Au film thickness and cross-sectional view SEM figures of its corresponding fabricated pseudoperiodic ARS after etching process: (a, e) 5 nm Au, (b, f) 7.5 nm Au, (c, g) 10 nm Au, and (d, h) 12.5 nm Au; (i) measured reflectance of the processed samples with different deposited Au film thickness.

process which would affect the dimension of the fabricated ARS, and similar etch rate of around 82 nm/minute was observed from all the samples. The aspect ratio increased slightly when the Au film thickness increased, which is caused by the larger thickness of the nano-islands. The average surface reflectance of the ARS fabricated with different Au film thickness have been measured and shown in Fig.. Although fairly low reflectance has been achieved with all the different Au film thickness, the lowest value of around 1.9 % is obtained with a Au film thickness of 10 nm.

Characterization of fluorescent SiC

The optimal Au film thickness and RIE conditions have then been applied on the N-B doped f-SiC sample with both N and B doping level higher than 10^{18} cm^{-3}. A relatively longer process time of 15 minutes was intentionally applied to achieve large etch depth. Fig. 5.14 shows the SEM images of the f-SiC sample at different process step. It is found that the pseudoperiodic ARS has a mean pitch of approximately 115 to 230 nm and the structure height varies from 400 to 850 nm.

The surface reflectance has been measured by using the calibrated goniometer system (see Fig. 3.6) at near-normal incidence of 6° over a wavelength range of 390-785 nm. The reflectance spectra are shown in Fig. 5.15, where the average surface reflectance is significantly suppressed from 20.5 % to 1.62 % by a factor of 11.6 after introducing the ARS. The reflectance at the luminescence peak (576 nm) is lower than 2 % and the minimum value of 0.05 % is obtained at 405 nm. Although the reflectance starts to increase at longer wavelength, the value through the whole measured spectral range is below 4 %. The antireflection performance of pseudoperiodic SiC ARS is quite comparable to the values of other reported periodic ARS. From the inset photograph of Fig. 5.15, it is also seen that the f-SiC surface turns from shiny light green color to dark greenblack color after introducing the ARS on the surface. Figs. 5.16a and 5.16b show the water contact angle measurements realized by using a drop shape analyzer (Krüss DSA 100S). The f-SiC surface turns from hydrophilic with a contact angle of 49° to hydrophobic with a contact angle of 98° after introducing the pseudoperiodic ARS, which is an appreciated merit for LED applications especially used at low temperature and in humid environment.

The ARPL measurement has been performed by using the same goniometer system, and a 377 nm laser beam from a diode laser has been

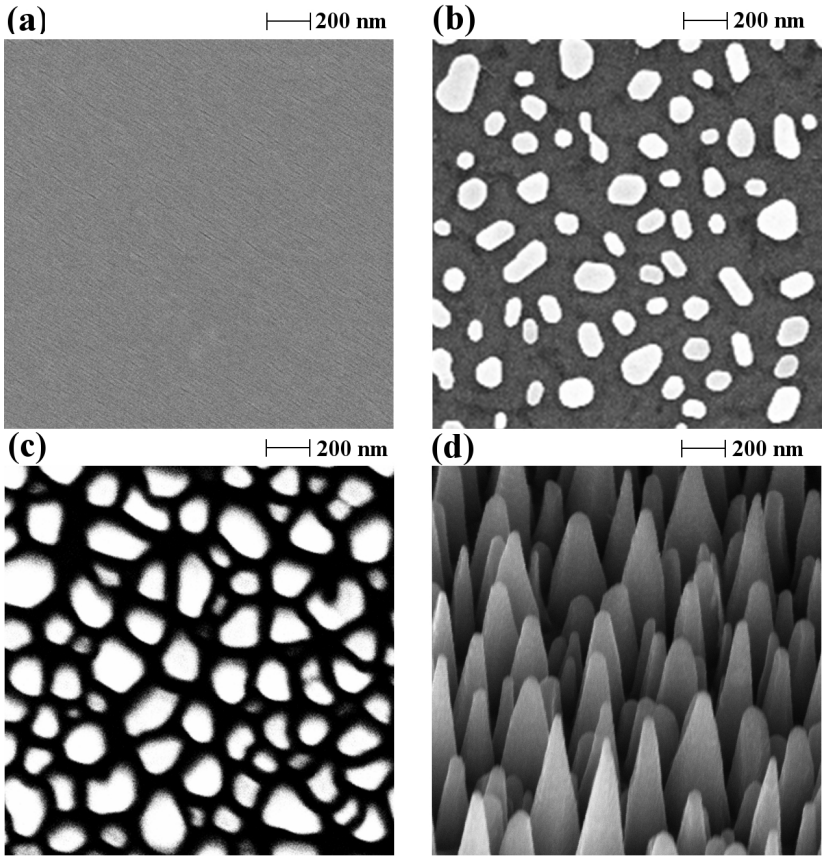

Figure 5.14: Top-view SEM figures of the SiC sample after (a) as-deposited of Au film, (b) RTP, and (c) RIE process; (d) an oblique-view SEM figure of the fabricated pseudoperiodic ARS.

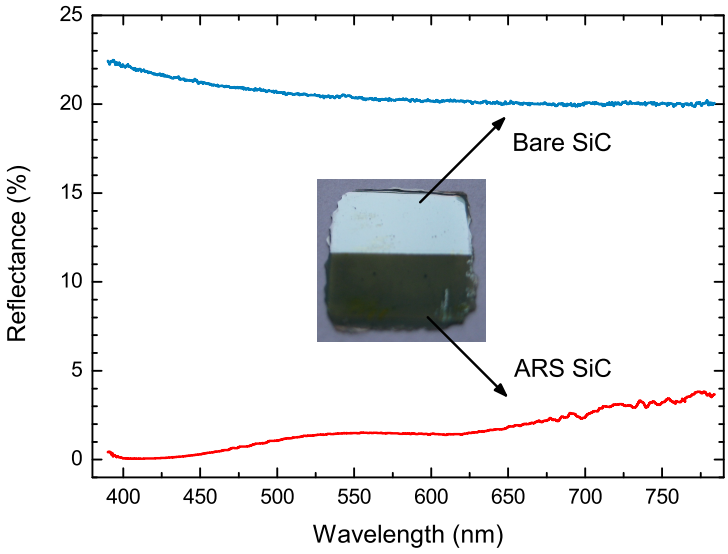

Figure 5.15: Surface reflectance of the bare and ARS SiC samples measured at near-normal incidence of 6°.

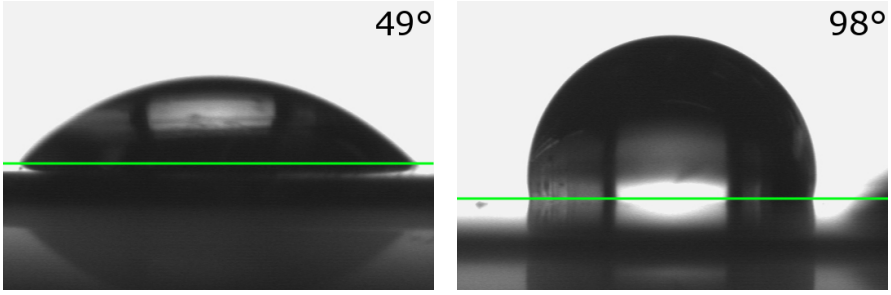

(a) **(b)**

Figure 5.16: Water droplet contact angle measurements on (a) bare SiC (49°) and (b) ARS SiC (98°).

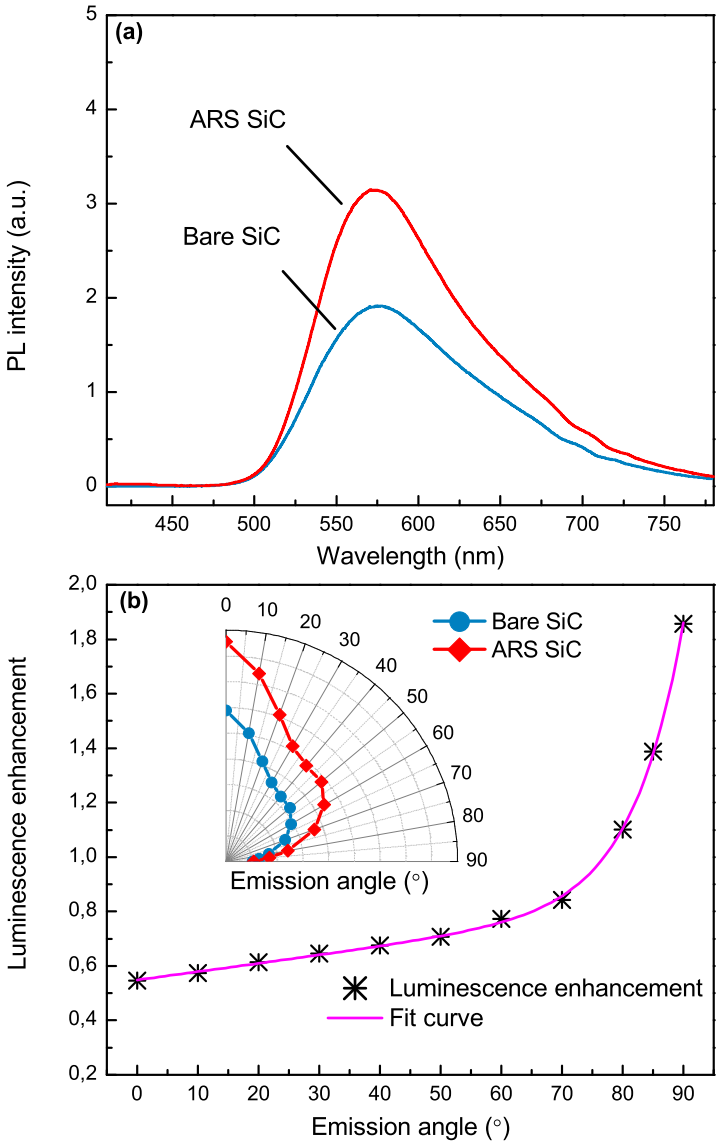

Figure 5.17: (a) Photoluminescence spectra of the bare and ARS SiC measured at 0°; (b) Luminescence enhancement of the SiC at different emission angle after introducing the ARS. Inset: spatial emission patterns for both bare and ARS SiC.

used as the excitation source. The sample was optically excited from its backside and the emission ARPL was measured from 0 (normal to the sample front surface) to 90° in steps of 10°. The photoluminescence spectra of the bare and ARS SiC measured at 0° are shown in Fig. 5.17(a). Broad DAP band luminescences with a peak wavelength of 576 nm and a full width at half maximum (FWHM) of around 110 nm are observed for both samples. The ARS SiC has a luminescence enhancement of 55 % at the emission angle of 0° which indicates a higher light extraction efficiency. This enhancement is probably due to the escape of the emitted light with an emission angle larger than the critical angle through the surface ARS.

Furthermore, the luminescence enhancement of f-SiC at different emission angle after introducing the ARS is presented in Fig. 5.17(b) where the ARS demonstrate the omnidirectional luminescence enhancement. The enhancement increased from 55 % at 0° to 186 % at 90°, and the integral luminescence enhancement in the whole range is 66.3 %. Spatial emission patterns of the two samples are shown in the inset of Fig. 5.17(b). It is seen that the spatial emission pattern is fairly preserved when the emission intensity is enhanced by introducing the pseudoperiodic ARS.

5.3.3 Conclusion

In conclusion, fabricating pseudoperiodic ARS on the f-SiC is a timesaving and effective method to achieve the surface antireflection in a large spectral range and omnidirectional luminescence enhancement. The average surface reflectance at 6° incidence is significantly decreased from 20.5 % to 1.62 % by a factor of 11.6 over the spectral range of 390-785 nm. The hydrophobic surface with a large water contact angle of 98° is obtained. The luminescence intensity is enhanced by 55 % at 0° emission angle and the enhancement further increased with a larger emission angle. The spatial emission pattern is fairly preserved from the ARPL measurement with an integral intensity enhancement of 66.3 %. It is shown that the pseudoperiodic ARS have comparable antireflection performance with other reported periodic structures and can improve the light extraction efficiency of f-SiC to a large extent and hence the external quantum efficiency of SiC-based white LEDs.

5.4 Summary

Three different fabrication methods are introduced here to form an ARS array on f-SiC. Periodic nanocone ARS made by using e-beam lithography can maintain the designed structure profile and thus achieve the desired spectral response. Nanosphere lithography is confirmed as an effective method to realize the periodic nanopatterning and nanodome ARS can be formed after a single-step dry etching process. Pseudoperiodic ARS array is fabricated by using self-assembled metal nano-particles as an etching template. The fabricated ARS made by different methods demonstrate a different structure profile, nevertheless, a low surface reflectance and an omnidirectional light extraction enhancement have been observed among all of these methods.

Chapter 6

Conclusion

Donor-Acceptor-Pair (DAP) recombination from the Fluorescent Silicon Carbide (f-SiC) demonstrates a broad spectral width by optical excitation. Combined luminescence spectra of Nitrogen-Boron (N-B) and Nitrogen-Aluminum (N-Al) co-doped f-SiC could cover the whole visible spectral range and are expected to have a good color rendering ability and long lifetime.

In this thesis, f-SiC samples with varied B and N doping concentrations were investigated in order to have a strong luminescence. It is found that a n-type doping sample is preferred to achieve an intense DAP emission while both B and N concentrations need to be larger than $10^{18}\ cm^{-3}$ as concluded from this study. Varied doping concentrations and types were also analyzed by longitudinal optical mode variation in their Raman spectra. From Angle-Resolved Photoluminescence (ARPL) study, it is seen that the luminescence intensity decreases as its emission angle increased. Luminescence peak shift is observed from the bare f-SiC sample which is attributed to the Fabry-Pérot microcavity interference effect.

Impact of applying surface Antireflective Structures (ARS) with different structure type and structure height on f-SiC based white Light-Emitting Diode (LED) have been theoretically examined. It is revealed that cylinder structures have a stronger influence on colorimetry performance of f-SiC based white LED. By applying cylinder structure, the spectra response can be controlled by designing the structure as a thin film interferometer. Therefore, a higher Color Rendering Index (CRI) could be achieved and the Correlated Color Temperature (CCT) could be modified in a very large range under stringent processing control. On

the other hand, cone structures have better performance to improve the light extraction efficiency over a broad spectral range, with a structure height larger than 400 nm. The CRI and CCT performance are very stable with varied structure dimension.

To minimize the surface reflection of f-SiC in a broad bandwidth, applying cone structures with varied structure profiles were examined in the spectral range of 350-800 nm. The results show that a high structure and a small period can lead to a relatively low surface reflectance. A low structure period to bottom diameter ratio value can also lead to a low reflectance within a large structure profile range. These calculation results provide a very useful guidance for ARS fabrication process. By applying cone structures with carefully designed structure profile, a low surface reflectance in a broad spectral range could be achieved.

A process method of fabricating a periodic ARS array on f-SiC has been developed in the cleanroom of DTU Danchip. By applying Electron beam (E-beam) lithography to make surface nanopattern as an etching mask and Reactive Ion Etching (RIE), a nanocone ARS array with designed profile can be fabricated. The surface reflectance over the whole visible spectral range is dramatically suppressed from 20.5 % of bare samples to 1.01 %. From the ARPL measurements, it is found that the luminescence intensity could be enhanced by more than 91 % in a very large emission angle range (up to 70°), while the largest enhancement of 115.4 % could be obtained at 16°. In addition, the Fabry-P*é*rot microcavity interference effect could be eliminated to preserve the luminescence spectral profile by introducing the ARS on f-SiC.

Another effective approach to fabricate a periodic nanodome ARS array is demonstrated on f-SiC by using nanosphere lithography and RIE processes. A polystyrene nanospheres array is self-assembly formed as an etching mask which is faster than normal nanopatterning method like e-beam lithography. A nanodome f-SiC array is obtained after the subsequent single-step RIE process. The average surface reflectance is significantly suppressed from 20.5 % to 3.3 % in the range of 390-785 nm and a large luminescence enhancement of 108.0 % is obtained at normal emission direction. Owing to the micro-lens shape, the nanodome structures can also confine the light transmission in the vertical direction. Experimental observations are then supported by numerical simulations.

Furthermore, a time-saving method of fabricating a pseudoperiodic ARS array by using self-assembled nanopatterned metal mask has been

demonstrated. In order to obtain the structure profile with the the lowest reflectance, both RIE conditions and deposited Au film thickness have been optimized. The optimal conditions are: RF power of 95 W, SF_6/O_2 flow rate of 18/4.5 sccm, chamber pressure of 30 mT, and 10 nm deposited Au film, which correspond to an etch rate of 82 nm/minute. The antireflection and light extraction performances of the pseudoperiodic ARS are comparable with the ones of the periodic ARS. Under the optimal etching conditions, the average surface reflectance of f-SiC in the spectral range of 390-785 nm is dramatically suppressed from 20.5 % to 1.62 %, and the hydrophobic surface with a large contact angle of 98° is also achieved. The ARPL study presents a considerable omnidirectional luminescence enhancement with an integral intensity enhancement of 66.3 % and a fairly preserved spatial emission pattern.

Significant surface reflection suppression and omnidirectional luminescence enhancement have been achieved on f-SiC by applying surface ARS. Mehods of fabricating ARS have been demonstrated and the results indicate that surface ARS is an ideal method to improve the light extraction efficiency in a broad spectral range.

The success of the above mentioned results have shown a promising future of f-SiC as an attractive wavelength-conversion material in white LED application. In order to further improve the quantum efficiency of the f-SiC, a better understanding of the recombination mechanism in f-SiC is required. More research efforts need to be devoted to the efficiency enhacement of the N-Al doped f-SiC. The growth conditions need to be optimized and well controlled to yield a better material quality. From the application point of view, surface ARS fabrication methods can be further explored to enhance the light extraction efficiency while the features of time-efficient and low-cost should be maintained. Finally, with the improvement of the overall effieciency, large-scale production of the f-SiC-based white LEDs can be expected.

Acronyms

ARPL Angle-Resolved Photoluminescence

ARS Antireflective Structures

CCT Correlated Color Temperature

CRI Color Rendering Index

CT Color Temperature

CVD Chemical Vapour Deposition

DAP Donor-Acceptor-Pair

E-beam Electron beam

FDTD Finite-Difference Time-Domain

FWHM Full Width at Half Maximum

f-SiC Fluorescent Silicon Carbide

GaN Gallium Nitride

HTCVD High Temperature Chemical Vapour Deposition

LED Light-Emitting Diode

LO Longitudinal Optical

LOPC Longitudinal Optical Plasmon Coupled

LPE Liquid Phase Epitaxial

N-Al Nitrogen-Aluminum

N-B Nitrogen-Boron

PEC Photoelectrochemical

PL Photoluminescence

PVT Physical Vapor Transport

RCWA Rigorous Coupled-Wave Analysis

RIE Reactive Ion Etching

RTP Rapid Thermal Processing

SiC Silicon Carbide

SIMS Secondary Ion Mass Spectrometry

UV Ultraviolet

Bibliography

[1] S. Kamiyama, T. Maeda, Y. Nakamura, M. Iwaya, H. Amano, I. Akasaki, H. Kinoshita, T. Furusho, M. Yoshimoto, T. Kimoto, J. Suda, A. Henry, I. G. Ivanov, J. P. Bergman, B. Monemar, T. Onuma, , and S. F. Chichibu, "Extremely high quantum efficiency of donor-acceptor-pair emission in N-and-B-doped 6H-SiC," Journal of Applied Physics **99** (2006).

[2] Y. Li, T. Gessmann, E. F. Schubert, and J. K. Sheu, "Carrier dynamics in nitride-based light-emitting p-n junction diodes with two active regions emitting at different wavelengths," Journal of Applied Physics **94**, 2167–2172 (2003).

[3] E. F. Schubert and J. K. Kim, "Solid-state light sources becoming smart," Science **308**, 1274–1278 (2005).

[4] I. Moreno and U. Contreras, "Color distribution from multicolor LED arrays," Optics Express **15**, 3607–3618 (2007).

[5] H. Yamamoto, "White led phosphors: the next step," Proceedings of SPIE p. 759808 (2010).

[6] P. Schlotter, R. Schmidt, and J. Schneider, "Luminescence conversion of blue light emitting diodes," Applied Physics A **64**, 417–418 (1997).

[7] X. Guo, J. Graff, and E. F. Schubert, "Photon recycling semiconductor light emitting diode," International Electron Devices Meeting pp. 600–603 (1999).

[8] E. F. Schubert, *Light Emitting Diodes* (Cambridge University Press, 2006), 2nd ed.

[9] C. Shen, K. Li, Q. long Hou, H. jun Feng, and X. yong Dong, "White LED based on YAG: Ce,Gd phosphor and CdSe-ZnS core/shell quantum dots," IEEE Photonics Technology Letters **22**, 884–886 (2010).

[10] H. Kuo, C. Hung, H. Chen, K. Chen, C. Wang, C. Sher, C. Yeh, C. Lin, C. Chen, and Y. Cheng, "Patterned structure of remote phosphor for phosphor-converted white LEDs," Optics Express **19**, A930–A936 (2011).

[11] R. Mueller-Mach, G. Mueller, M. R. Krames, H. A. Höppe, F. Stadler, W. Schnick, T. Juestel, , and P. Schmidt, "Highly efficient all-nitride phosphor-converted white light emitting diode," Physica Status Solidi (A) **202**, 1727–1732 (2005).

[12] C. Chang, C. Chen, C. Wu, S. Chang, J. Hung, and Y. Chi, "High-color-rendering pure-white phosphorescent organic light-emitting devices employing only two complementary colors," Organic Electronics **11**, 266–272 (2010).

[13] H. Menkara, R. A. Gilstrap, T. Morris, M. Minkara, B. K. Wagner, and C. J. Summers, "Development of nanophosphors for light emitting diodes," Optics Express **19**, A972–A981 (2011).

[14] Y. S. Park, *SiC Materials and Devices*, vol. 52 (Academic Press, 1998).

[15] H. Matsunami, "Technological breakthroughs in growth control of silicon carbide for high power electronic devices," Japanese Journal of Applied Physics **43**, 6835–6847 (2004).

[16] G. R. Fishe and P. Barnes, "Towards a unified view of polytypism in silicon carbide," Philosophical Magazine B **61**, 217–236 (1990).

[17] J. B. Casady and R. W. Johnson, "Status of silicon carbide (SiC) as a wide-bandgap semiconductor for high-temperature applications: a review," Solid-State Electronics **39**, 1409–1422 (1996).

[18] A. Taylor and R. M. Jones, *Silicon Carbide - A High Temperature Semiconductor* (Pergamon Press: Oxford, 1960).

[19] R. W. G. Wyckoff, *Crystal Structures*, vol. 1 (John Wiley & Sons, New York, 1963).

[20] Y. M. Tairov and V. F. Tsvetkov, *Progress in Crystal Growth and Characterization* (Pergamon Press: Oxford, 1983).

[21] N. W. Thibault, "Morphological and structural crystallography and optical properties of silicon carbide," American Mineralogist **29**, 327 (1944).

[22] E. L. Kern, D. W. Hamill, H. W. Deem, and H. D. Sheets, "Thermal properties of beta silicon carbide from 20 to 2000 C," Materials Research Bulletin **4**, S25 (1969).

[23] Cree, "Properties and specifications for 4H-silicon carbide," Tech. Rep. 10.95, Cree Research Inc. (1995).

[24] Cree, "Properties and specifications for 6H-silicon carbide," Tech. Rep. 10.95, Cree Research Inc. (1995).

[25] Y. Chinone, S. Ezaki, F. Fuijta, and R. Matsumoto, "Amorphous and crystalline silicon carbide and related materials 2," Springer Proceedings in Physics **43**, 198 (1989).

[26] S. Karmann, R. Helbig, and R. A. Stein, "Piezoelectric properties and elastic constants of 4H and 6H sic at temperatures 4-320 K," Journal of Applied Physics **66**, 3922–3924 (1989).

[27] D. Morelli, J. Hermans, C. Beetz, W. S. Woo, G. L. Harris, and C. Taylor, "Carrier concentration dependence of the thermal conductivity of silicon carbide," Proceedings of the 5th International Silicon Carbide and Related Materials Conference **1-3**, 313–315 (1993).

[28] G. A. Slack, "Thermal conductivity of pure and impure silicon, silicon carbide, and diamond," Journal of Applied Physics **35**, 3460–3466 (1964).

[29] G. L. Harris, *Properties of Silicon Carbide*, vol. 13 of *EMIS datareview* (INSPEC: London, 1995).

[30] Cree, "Properties and specifications of silicon carbide," Tech. Rep. 10.95, Cree Research Inc. (1995).

[31] V. Dmitriev, T. P. Chow, S. P. DenBaars, M. S. Shur, M. G. Spencer, and G. White, "High-temperature electronics in europe," Tech. rep., International Technology Research Institute (2000).

[32] J. A. Lely, "Darstellung von einkristallen von silicium carbid und beherrschung von art und menge der eingebauten verunreinigungen," Berichte der Deutschen Keramischen Gesellschaft **32**, 229–236 (1955).

[33] A. A. Glagovski, E. V. Grankovski, A. K. Drozdov, V. M. Efimov, G. Y. Skrinnikova, B. V. Smirnov, M. G. Travadgan, M. P. Chetkov, and V. A. Shevchenko, *Problems of Physics and Technology of Wide Band Gap Semiconductors* (LIYaF, Leningrad, 1980).

[34] W. F. Knippenberg, "Growth phenomena in silicon carbide," Tech. Rep. 18, Philips Research Reports (1963).

[35] V. A. Dmitriev, P. A. Ivanov, Y. V. Morozenko, V. E. Chelnokov, and A. E. Cherenkov, "Silicon carbide devices for active electronics and optoelectronics," Applications of Diamond Films and Related Materials pp. 769–774 (1991).

[36] M. M. Anikin, P. A. Ivanov, A. A. Lebedev, S. N. Pyatko, A. M. Strelchuk, and A. L. Syrkin, *Semiconductor Interfaces and Microstructures* (World Scientific Publishing Co., NJ, USA, 1993), chap. High-temperature discrete in 6H-SiC: sublimation epitaxial growth, device technology and electrical performance, pp. 280–311.

[37] R. B. Campbell and Y. C. Chang, *Semiconductors and Semimetals*, vol. 7B (Academic, San Diego, USA, 1971).

[38] Y. M. Tairov and V. F. Tsvetkov, "Investigation of growth processes of ingots of silicon carbide single crystals," Journal of Crystal Growth **43**, 209–212 (1978).

[39] Y. M. Tairov and V. F. Tsvetkov, "General principles of growing large-size single crystals of various silicon carbide polytypes," Journal of Crystal Growth **52**, 146–150 (1981).

[40] D. L. Barrett, R. G. Seidensticker, W. Gaida, R. H. Hopkins, and W. J. Choyke, "Sublimation vapor transport growth of silicon carbide," Springer Proc. in Physics **56**, 33–39 (1992).

[41] S. N. Gorin and A. A. Pletyushkin, "Crystal structure peculiaities of cubic silicon carbide crystals obtained from a gas phase," Izvestiya Akademii Nauk SSSR, Seriya Fizicheskaya **28**, 1310–1315 (1964).

[42] Kordina, Hallin, Ellison, Bakin, Ivanov, Henry, Yakimova, Touminen, Vehanen, and Janzen, "High temperature chemical vapor deposition of SiC," Applied Physics Letters **69**, 1546–1548 (1996).

[43] S. E. Saddow and A. Agarwal, *Advances in Silicon Carbide Processing and Applications* (Artech House, Inc., 2004).

[44] R. C. Marshall, "Growth of silicon carbide from solution," Materials Research Bulletin **4**, S37–S84 (1969).

[45] W. E. Nelson, F. A. Halden, and A. Rosengreen, "Growth and properties of beta-SiC single crystals," Journal of Applied Physics **37**, 333–336 (1966).

[46] G. A. Wolff, B. N. Das, C. B. Lamport, A. I. Mlavsky, and E. A. Trickett, "Principles of solution and traveling solvent growth of silicon carbide," Materials Research Bulletin **4**, S67–S72 (1969).

[47] R. Yakimova, M. Tuominen, A. S. Bakin, J. O. Fornall, A. Vehanen, and E. Janzen, "Silicon carbide liquid phase epitaxy in the Si-Sc-C system," Proceedings of the 6th International Silicon Carbide and Related Materials Conference pp. 101–104 (1995).

[48] Yole, "SiC 2010 report: How SiC will impact electronics: A 10 years projection," Tech. rep., Yole Developpement (2009).

[49] J. Ooshita and N. Microdevices, "Nippon steel enters SiC wafer business," Tech. rep., Tech news - straight from Asia (2009).

[50] D. Hofmann, E. Schmitt, M. Bickermann, M. Kölbl, P. Wellmann, and A. Winnacker, "Analysis on defect generation during the SiC bulk growth process," Materials Science and Engineering: B **61-62**, 48–53 (1999).

[51] R. Giocondi, G. S. Rohrer, M. Skowronski, V. Balakrishna, G. Augustine, H. M. Hobgood, and R. H. Hopkins, "The relationship between micropipes and screw dislocations in pvt grown 6H-SiC," MRS Proceedings p. 539 (1996).

[52] J. Heindl, W. Dorsch, H. P. Strunk, S. G. Müller, R. Eckstein, D. Hofmann, and A. Winnacker, "Dislocation content of micropipes in SiC," Physical Review Letters **80**, 740–741 (1998).

[53] X. R. Huang, M. Dudley, W. M. Vetter, W. Huang, S. Wang, and C. H. C. Jr., "Direct evidence of micropipe-related pure superscrew dislocations in SiC," Applied Physics Letters **74**, 353–356 (1999).

[54] P. Pirouz, "The origin of nanopipes and micropipes in non-cubic GaN and SiC," MRS Proceedings p. 113 (1998).

[55] H. Yamaguchi, S. Nishizawa, W. Bahng, K. Fukuda, S. Yoshida, K. Arai, and Y. Takano, "Reflection and transmission X-ray topographic study of a SiC crystal and epitaxial wafer," Materials Science and Engineering: B **61-62**, 221–224 (1999).

[56] S. Nishizawa, H. Yamaguchi, T. Kato, N. Oyanagi, S. Yoshida, and K. Arai, "Development of X-ray topography system for in-situ observation of sublimation SiC single crystal growth," Bulletin of the Electrotechnical Laboratory **63**, 305–310 (1999).

[57] M. S. Ramm, E. N. Mokhov, S. E. Demina, M. G. Ramm, A. D. Roenkov, Y. A. Vodakov, A. S. Segal, A. N. Vorobev, S. Y. Karpov, A. V. Kulik, and Y. N. Makarov, "Optimization of sublimation growth of SiC bulk crystals using modeling," Materials Science and Engineering: B **61-62**, 107–112 (1999).

[58] P. G. Neudeck, W. Huang, and M. Dudley, "Breakdown degradation associated with elementary screw dislocations in 4H-SiC p+n junction rectifiers," Solid-State Electronics **42**, 2157–2164 (1998).

[59] N. Schulze, D. L. Barrett, G. Pensl, S. Rohmfeld, and M. Hundhausen, "Near-thermal equilibrium growth of SiC by physical vapor transport," Materials Science and Engineering: B **61-62**, 44–47 (1999).

[60] Y. A. Vodakov and E. N. Mokhov, *USSR Patent N7062320* (USSR Patent, 1970).

[61] P. A. Icanov and V. E. Chelnokov, "Semiconductor silicon caridetechnology and devices: A review," Semiconductors **29**, 1003–1013 (1995).

[62] D. J. Larkin, "An overview of SiC epitaxial growth," MRS Bulletin **22**, 36–40 (1997).

[63] S. Jang, T. Kimoto, and H. Matsunami, "Deep levels in 6H-SiC wafers and step-controlled epitaxial layers," Applied Physics Letters **65**, 581–583 (1994).

[64] A. Itoh, H. Akita, T. Kimoto, and H. Matsunami, "High-quality 4H-SiC homoepitaxial layers grown by step-controlled epitaxy," Applied Physics Letters **65**, 1400–1402 (1994).

[65] S. V. Rendakova, I. P. Nikitina, A. S. Tregubova, and V. A. Dmitriev, "Micropipe and dislocation density reduction in 6H-SiC and 4H-SiC structures grown by liquid phase epitaxy," Journal of Electronic Materials **27**, 292–295 (1998).

[66] R. C. Marshall, J. W. Faust, and C. E. Ryan, *Silicon Carbide* (University of South Carolina Press, 1973).

[67] J. W. Palmour, R. F. Davis, T. M. Wallett, and K. B. Bashin, "Dry etching of β-SiC in CF_4 and CF_4+O_2 mixtures," Journal of Vacuum Science and Technology A **4**, 590–593 (1986).

[68] G. Kelner, S. C. Binari, and P. H. Klein, "Plasma etching of β-SiC," Journal of The Electrochemical Society **134**, 253–254 (1987).

[69] J. Sugiura, Y. W. Lu, K. C. Kadien, and A. J. Steckl, "Reactive ion etching of SiC thin films using fluorinated gases," Journal of Vacuum Science and Technology B **4**, 349–354 (1986).

[70] I. Lauermann, D. Meissner, R. Memming, R. Reineke, and B. Kastening, *Electrochemie in Energie- und Umwelttechnik* (VCH, Weinheim, 1991).

[71] H. J. Round, "A note on carborundum," Electrical World **19**, 879 (1907).

[72] J. Shimada, Y. Kawakami, and S. Fujita, "Development of lighting goggle with power white led modules," SPIE Photonics West **4996** (2003).

[73] G. Rostky, "LEDs cast monsanto in unfamiliar role," Electronic Engineering Times **944** (1997).

[74] Osram Opto Semiconductors, "Leds bridge time and space," Press release (2004).

[75] D. Corell, H. Ou, C. Dam-Hansen, P. Petersen, and D. Friis, "Light emitting diodes as an alternative ambient illumination source in photolithography environment," Optics Express **17**, 17293–17302 (2009).

[76] D. A. B. Miller, *Course Notes for EE243 Semiconductor Optoelectronic Devices* (Stanford University, 2000).

[77] M. Ikeda, H. Matsunami, and T. Tanaka, "Site effect on the impurity levels in 4H, 6H, and 15R SiC," Physical Review B **22**, 2842–2854 (1980).

[78] M. Ikeda, H. Matsunami, and T. Tanaka, "Site-dependent donor and acceptor levels in 6H-SiC," Journal of Luminescence **20**, 111–129 (1979).

[79] Y. Vodakov, A. Volfson, , G. Zaritskil, E. Mokhov, A. Ostroumov, A. Roenkov, V. Semenov, V. Sokolov, V. Syralev, and V. Udaltsov, "Efficient green-emitting silicon carbide diodes," Soviet Physics Semiconductors **26**, 59–61 (1992).

[80] A. S. Barash, Y. Vodakov, E. Koltsova, A. Maltsev, E. Mokhov, and A. Roenkov, "Green LEDs made from heteroepitaxial layers of silicon carbide of the 4H polytype," Soviet Technical Physics Letters **14**, 964–965 (1988).

[81] B. Vishnevskaya, V. A. Dmitriev, I. D. Kovalenko, L. M. Kogan, Y. V. Morozenko, A. L. Sirkin, B. V. Tsarenkov, and V. E. Chelnokov, "Blue light emitting diodes on SiC-6H," Soviet Physics Semiconductors **22**, 664 (1988).

[82] L. Hoffman, G. Ziegler, D. Theis, and C. Weyrich, "Silicon carbide blue light emitting diodes with improved external quantum efficiency," Journal of Applied Physics **53**, 6962–6967 (1982).

[83] J. Edmond, H. Kong, and C. Carter, "Blue LEDs, uv photodiodesand high-temperature rectifiers in 6H-SiC," Physica B **185**, 453–460 (1993).

[84] J. Edmond, H. Kong, A. Suvorov, D. Waltz, and C. Carter, "6h-silicon carbide light emitting diodes and uv photondiodes," Physica Status Solidi (A) **162**, 481–491 (1997).

[85] V. M. Gusev and K. D. Demakov, "Electro-luminescence properties of several SiC polytypes, ion doped by Al," Soviet Physics Semiconductors **15**, 1413 (1981).

[86] V. A. Dmitriev, "Silicon carbide light-emitting diodes for the blue-violet region," Soviet Technical Physics Letters **11**, 101–102 (1985).

[87] V. A. Dmitriev, L. Kogan, V. Morozenko, B. V. Tsarenkov, V. E. Chelnokov, and A. E. Cherenkov, "Violet-light-emitting SiC-4H diodes," Soviet Physics Semiconductors **23**, 23–25 (1989).

[88] A. A. Kalnin, Y. M. Tairov, and D. A. Yuskov, "Luminescence of silicon carbide containing beryllium impurity," Soviet Physics Solid State **8**, 755 (1966).

[89] Y. A. Vodakov and E. N. Mokhov, *Silicon Carbide* (University of South Carolina Press, Columbia, SC, 1974), chap. Diffusion And Solubility Of Impurities In Silicon Carbide, p. 508.

[90] M. Syväjärvi and R. Yakimova, *Encyclopedia - the Comprehensive Semiconductor Science and Technology* (Elsevier, 2011), chap. Sublimation epitaxial growth of hexagonal and cubic SiC.

[91] D. R. Hamilton, W. J. Choyke, and L. Patrick, "Photoluminescence of nitrogen-exciton complexes in 6H SiC," Physical Review **131**, 127–133 (1963).

[92] W. J. Choyke, D. R. Hamilton, and L. Patrick, "Optical properties of cubic SiC: luminescence of nitrogen-exciton complexes, and interband absorption," Physical Review **133**, 1163–1166 (1964).

[93] M. Ohishi, "Time-resolved studies on recombination luminescence of donor-acceptor pairs in ZnSe," Japanese Journal of Applied Physics **25**, 1546–1551 (1986).

[94] P. Bäume, F. Kubacki, and J. Gutowski, "Characterization of impurities in II-VI semiconductors by time-resolved lineshape analysis of donor-acceptor pair spectra," Journal of Crystal Growth **138**, 266–273 (1994).

[95] V. Grivickas, K. Gulbinas, V. Jokubavicius, Y. Ou, H. Ou, M. Linnarsson, M. Syväjärvi, and S. Kamiyama, "Carrier lifetimes in

fluorescent 6H-SiC for LEDs application," Proceedings of 39th Lithuanian National Physics Conference p. 4 (2011).

[96] Y. Cheng, G. Lee, P. Chou, L. Chen, Y. Chi, C. Yang, Y. Song, S. Chang, P. Shih, and C. Shu, "Rational design of chelating phosphine functionalized Os^{II} emitters and fabrication of orange polymer light-emitting diodes using solution process," Advanced Functional Materials **18**, 183–194 (2008).

[97] J. Kim, P. Jeon, Y. Park, J. Choi, H. Park, G. Kim, and T. Kim, "White-light generation through ultraviolet-emitting diode and white-emitting phosphor," Applied Physics Letters **85**, 3696–3698 (2004).

[98] X. Li, Z. Chen, and E. Shi, "Effect of doping on the Raman scattering of 6H-SiC crystals," Physica B **405**, 2423–2426 (2010).

[99] G. Irmer, V. V. Toporov, B. H. Bairamov, and J. Monecke, "Determination of the charge carrier concentration and mobility in n-GaP by Raman spectroscopy," Physica Status Solidi (B) **119**, 595–603 (1983).

[100] H. Yugami, S. Nakashima, A. Mitsuishi, A. Uemoto, M. Shigeta, K. Furukawa, A. Suzuki, and S. Nakajima, "Characterization of the free-carrier concentrations in doped β-SiC crystals by Raman scattering," Journal of Applied Physics **61**, 354–358 (1987).

[101] D. Sotta, E. Hadji, N. Magnea, E. Delamadeleine, P. Besson, P. Renard, and H. Moriceau, "Resonant optical microcavity based on crystalline silicon active layer," Journal of Applied Physics **92**, 2207–2209 (2002).

[102] S. S. Pan, C. Ye, X. M. Teng, and G. H. Li, "Angle-dependent photoluminescence of [110]-oriented nitrogen-doped SnO_2 films," Journal of Physics D **40**, 4771–4774 (2007).

[103] J. Q. Xi, M. F. Schubert, J. K. Kim, E. F. Schubert, M. Chen, S.-Y. Lin, W. Liu, and J. A. Smart, "Optical thin-film materials with low refractive index for broadband elimination of fresnel reflection," Nature Photonics **1**, 176–179 (2007).

[104] X. Li, J. Gao, L. Xue, and Y. Han, "Porous polymer films with gradient-refractive-index structure for broadband and omnidirectional antireflection coatings," Advanced Functional Materials **20**, 259–265 (2010).

[105] S. A. Boden and D. M. Bagnall, "Tunable reflection minima of nanostructured antireflective surfaces," Applied Physics Letters **93**, 133108 (2008).

[106] T. Fujii, Y. Gao, R. Sharma, E. L. Hu, S. P. DenBaars, and S. Nakamura, "Increase in the extraction efficiency of GaN-based light-emitting diodes via surface roughening," Applied Physics Letters **84**, 855–857 (2004).

[107] H.-Y. Lee, Y.-H. Chou, C.-T. Lee, W.-Y. Yeh, and M.-T. Chu, "Mechanisms of lighting enhancement of Al nanoclusters-embedded Al-doped ZnO film in GaN-based light-emitting diodes," Journal of Applied Physics **107**, 014503 (2010).

[108] S. Fan, P. R. Villeneuve, and J. D. Joannopoulos, "High extraction efficiency of spontaneous emission from slabs of photonic crystals," Physical Review Letters **78**, 3294–3297 (1997).

[109] K. Bergenek, C. Wiesmann, R. Wirth, L. O′Faolain, N. Linder, K. Streubel, and T. F. Krauss, "Enhanced light extraction efficiency from AlGaInP thin-film light-emitting diodes with photonic crystals," Applied Physics Letters **93**, 041105 (2008).

[110] K. McGroddy, A. David, E. Matioli, M. Iza, S. Nakamura, S. DenBaars, J. S. Speck, C. Weisbuch, and E. L. Hu, "Directional emission control and increased light extraction in GaN photonic crystal light emitting diodes," Applied Physics Letters **93**, 103502 (2008).

[111] K. Kim, J. Choi, J. B. Park, S. C. Jeon, J. S. Kim, and H. M. Lee, "Lattice constant effect of photonic crystals on the light output of blue light-emitting diodes," IEEE Photonics Technology Letters **20**, 1455–1457 (2008).

[112] S. Noda and M. Fujita, "Photonic crystal efficiency boost," Nature Photonics **3**, 129–130 (2009).

[113] S. J. An, J. H. Chae, G.-C. Yi, and G. H. Park, "Enhanced light output of GaN-based light-emitting diodes with ZnO nanorod arrays," Applied Physics Letters **92**, 121108 (2008).

[114] M.-K. Lee, C.-L. Ho, and P.-C. Chen, "Light extraction efficiency enhancement of GaN blue LED by liquid-phase-deposited ZnO rods," IEEE Photonics Technology Letters **20**, 252–254 (2008).

[115] K.-K. Kim, S. dong Lee, H. Kim, J.-C. Park, S.-N. Lee, Y. Park, S.-J. Park, and S.-W. Kim, "Enhanced light extraction efficiency of GaN-based light-emitting diodes with ZnO nanorod arrays grown using aqueous solution," Applied Physics Letters **94**, 071118 (2009).

[116] S. L. Diedenhofen, G. Vecchi, R. E. Algra, A. Hartsuiker, O. L. Muskens, G. Immink, E. P. A. M. Bakkers, W. L. Vos, and J. G. Rivas, "Broad-band and omnidirectional antireflection coatings based on semiconductor nanorods," Advanced Materials **21**, 973–978 (2009).

[117] C.-H. Sun, P. Jiang, and B. Jiang, "Broadband moth-eye antireflection coatings on silicon," Applied Physics Letters **92**, 061112 (2008).

[118] Y. M. Song, E. S. Choi, J. S. Yu, and Y. T. Lee, "Light-extraction enhancement of red AlGaInP light-emitting diodes with antireflective subwavelength structures," Optics Express **17**, 20991–20997 (2009).

[119] E. B. Grann, M. G. Moharam, and D. A. Pommet, "Optimal design for antireflective tapered two-dimensional subwavelength grating structures," Journal of the Optical Society of America A **12**, 333–339 (1995).

[120] D. Lehr, M. Helgert, M. Sundermann, C. Morhard, C. Pacholski, J. P. Spatz, and R. Brunner, "Simulating different manufactured antireflective sub-wavelength structures considering the influence of local topographic variations," Optics Express **18**, 23878–23890 (2010).

[121] H. Park, D. Shin, G. Kang, S. Baek, K. Kim, and W. J. Padilla, "Broadband optical antireflection enhancement by integrating antireflective nanoislands with silicon nanoconical-frustum arrays," Advanced Materials **23**, 5796–5800 (2011).

[122] R. Sanatinia, K. M. Awan, S. Naureen, N. Anttu, E. Ebraert, and S. Anand, "Gaas nanopillar arrays with suppressed broadband

reflectance and high optical quality for photovoltaic applications," Optical Materials Express **2**, 1671–1679 (2012).

[123] J. Zhu, C.-M. Hsu, Z. Yu, S. Fan, and Y. Cui, "Nanodome solar cells with efficient light management and self-cleaning," Nano Letters **10**, 1979–1984 (2010).

[124] B. M. Phillips, P. Jiang, and B. Jiang, "Biomimetic broadband antireflection gratings on solar-grade multicrystalline silicon wafers," Applied Physics Letters **99**, 191103 (2011).

[125] T. Wei, K. Wu, D. Lan, Q. Yan, Y. Chen, C. Du, J. Wang, Y. Zeng, and J. Li, "Selectively grown photonic crystal structures for high efficiency InGaN emitting diodes using nanospherical-lens lithography," Applied Physics Letters **101**, 211111 (2012).

[126] W. Y. Fu, K. K.-Y. Wong, and H. W. Choi, "Close-packed hemiellipsoid arrays: A photonic band gap structure patterned by nanosphere lithography," Applied Physics Letters **95**, 133125 (2009).

[127] Y.-C. Chang, S.-M. Wang, H.-C. Chung, C.-B. Tseng, and S.-H. Chang, "Observation of absorption-dominated bonding dark plasmon mode from metal-insulator-metal nanodisk arrays fabricated by nanospherical-lens lithography," ACS Nano **6**, 3390–3396 (2012).

[128] R. Y. Zhang, B. Shao, J. R. Dong, K. Huang, Y. M. Zhao, S. Z. Yu, and H. Yang, "Broadband quasi-omnidirectional antireflection algainp window for III-V multi-junction solar cells through thermally dewetted Au nanotemplate," Optical Materials Express **2**, 173–182 (2012).

[129] J. W. Leem and J. S. Yu, "Wafer-scale highly-transparent and superhydrophilic sapphires for high-performance optics," Optics Express **20**, 26160–26166 (2012).

[130] J. W. Leem and J. S. Yu, "Broadband and wide-angle antireflection subwavelength structures of si by inductively coupled plasma etching using dewetted nanopatterns of au thin films as masks," Thin Solid Films **519**, 3792–3797 (2011).